ABSTRACT

CLARK, DAVID HAMILTON. Ion Energy Distribution Functions Using Multi-frequency Harmonic Drive. (Under the direction of Dr. Steven Shannon).

Multi-frequency RF power delivery for IEDF control has become commonplace in semiconductor manufacturing, particularly in plasma etch applications. Recently, two frequency drives where the higher drive frequency is a harmonic of the lower drive frequency have shown interesting influence on IEDF's with phase acting as an additional tuning knob for control. In this work, an RF sheath model that assumes a matrix sheath condition and known electron density is used to compare the influence of multiple frequencies over transient sheath parameters, specifically the time dependent potential across the powered sheath. Using this time dependent potential, ion energies incident on the plasma facing surface are calculated using an ion transit time dependent dampening term. Ion energy distribution functions are obtained for dual frequency conditions where the one frequency is an integer multiple of the other and compared to the more typical case where the frequencies do not have an integer multiple relationship. Control of the distribution width is identical with respect to relative RF current from two sources for both the integer and non-integer case. The integer frequency relationship produces (n-1) intermediate peaks in the distribution between the maximum and minimum energies whose energy and magnitude can be controlled with the relative phase of the two waveforms. Manipulation of the phase and amplitude of these two power sources can also produce some useful distribution functions, in some cases mimicking distributions that are normally achieved outside of the range of frequencies used to drive the sheath potential, and lend an additional level of IEDF control not achievable with comparable non-integral dual frequency drives. This work offers a brief review of dual frequency IEDF control and presents a model that captures the effects of both frequency mixing and phase of integer multiple frequency drives.

Ion Energy Distribution Functions Using Multi-frequency Harmonic Drive

by
David Hamilton Clark

A thesis submitted to the Graduate Faculty of
North Carolina State University
in partial fulfillment of the
requirements for the degree of
Master of Science

Nuclear Engineering

Raleigh, North Carolina

2013

APPROVED BY:

Dr. S. C. Shannon
Chair of Advisory Committee

Dr. M. A. Bourham

Dr. J. G. Gilligan

Biography

David Hamilton Clark was born on May 7, 1986 to Margaret H. Wagers and David J. Clark. He was raised in Charlotte, North Carolina and graduated from high school at The Asheville School in 2005. He then which he attended Elon University from which he graduated in May, 2009 with a B.S. in Physics. That Fall he began pursuit of a graduate degree in Nuclear Engineering at North Carolina State University.

Acknowledgements

I would like to express my appreciation to my advisory committee: Dr. Steven C. Shannon and Dr. Mohamed A. Bourham. Thanks for giving me the opportunity to be part of the Plasma research. It has been a pleasure working with Dr. Bourham, who made this study possible by providing the lab equipment necessary to run experiments. Also, thanks to MKS Instruments Inc. for donating the diagnostic equipment for this project. My gratitude also goes to the NC State Precision Machine Shop, as there are not enough words to describe its excellent work. Brandon Byrns, Elijah Martin, Adam Steiner, Alex Lindsay, and Chris Hardimann, thank you for all your help and guidance throughout my lengthy education at NC State. I would not have finished without you. Special acknowledgement goes to Hermine Kabbendjan; your guidance in both undergraduate and graduate school was invaluable to my success. Thanks to the Nanofabrication Facility at NCSU for providing me an opportunity to learn the basics of PECVD and vacuum chamber procedures. Also thanks to my peers for their help: Tony McWilliams, Levon Keusseyan, and Brian Froese.

Table of Contents

List of Figures

List of Tables

List of Symbols and Abbreviations

n_e	electron density	cm^{-3}	per cubic centimeter
T_e	electron temperature	eV	electron-volts
V_{dc}	DC voltage	V	volts
m_i	ion mass	kg	kilogram
φ	phase	° or radian	degrees
I_{low}	low current	A	Amps
I_{high}	high current	A	Amps
f_{low}	low frequency	MHz	Megahertz
f_{high}	high frequency	MHz	Megahertz
x	contribution ratio of f_{low} to f_{high}	%	percent
n_g	neutral gas density	cm^{-3}	per cubic centimeter
α_R	relative polarizability	N/A	#
ν	collision frequency	Hz	hertz
P_{low}	Low Power input	W	Watts
P_{high}	High Power input	W	Watts
Area	Electrode Area	mm^2	millimeters squared
s_{low}	sheath parameter	m	meters
s_{high}	sheath parameter	m	meters
τ_i	Ion transit time	s	seconds
V_{sheath}	Sheath voltage	V	Volts
ω	frequency	Hz	hertz
t	time	s	seconds
ε_0	permittivity of free space	8.8542×10^{-12}	F/m
n	harmonic of frequency	N/A	#
Z	Impedance	Ω	ohms
L	Inductance	H	Henry
k	Boltzmann constant	1.3807×10^{-23}	J/K
e	elementary charge	1.6022×10^{-19}	C
E	Electric field	V/M	volts per meter
IEDF	Ion Energy Distribution Function		
CCP	Capacitively Coupled Plasma		
ICP	Inductively Coupled Plasma		
2f-CCPs	Dual Frequency Capacitively Coupled Plasmas		
MEMS	Micro-electromechanical systems		
ALD	Atomic Layer Deposition		
CVD	Chemical Vapor Deposition		
PECVD	Plasma Enhanced Chemical Vapor Deposition		
DC	Direct Current		
AC	Alternating Current		
RFEA	Retarding Field Energy Analyzer		
VHF	Very High Frequency (13MHz – 90MHz)		

Ar	Argon gas
RF	Radio Frequency
UV	Ultra-Violet
VNA	Vector Network Analyzer
VI Probe	Voltage – Current Probe
PSR	Plasma Series Resonance
PROES	Phase Resolved Optical Emission Spectroscopy

PURPOSE

Plasma etching for use in the fabrication of integrated circuits (IC) was introduced in the 1970s as a technique for removing resistive layers from a material's surface. By the 1980s the technique had improved to the point where it was used to etch features into materials and define the individual components of solid state devices. The technique was originally called Reactive Ion Etching (RIE). As time passed more complex and varied techniques developed. These complex techniques employed the same fundamental physics as the original RIE systems, albeit with more complex plasma source designs to obtain the necessary conditions to optimize process conditions. These systems were typically named after their plasma source technologies and included ECR (electron cyclotron resonance), ICP (inductively coupled plasma), and CCP (capacitively coupled plasma).

The most commercially significant use of plasma etching has been in the semiconductor industry to make microprocessors. Plasma processing techniques led to the rapid micro-sizing of consumer electronics in the late nineties, allowing pattern transfer to keep pace with advances in photolithographic techniques for defining device features.

Plasmas are also commonly used for deposition of materials that make up integrated circuit devices. PECVD (plasma enhanced chemical vapor deposition) uses plasma discharges to decompose gases at low temperatures, enabling deposition of materials on substrates that were otherwise not possible due to low temperature requirements such as plastics.

New plasma applications are being explored in a variety of fields, from military to medical to environmental protection. For example, plasmas are being developed as a sterilization mechanism for both medical instruments and wound healing. There are also plasmas designed to cut down on pollution by neutralizing certain harmful components in exhaust. Portable plasma generating tools are in development in the military as a means to stimulate damaged human tissue to heal itself much more quickly for injured soldiers on the battlefield. NASA has been developing cleaning processes that will eventually be applied to Mars-bound probes that will fully cleanse them of all microbial life as a precaution to prevent bringing life to other planets by accident from our own world.

As the primary application of plasma is to manufacture microelectronics, this work will focus on the specific manufacturing step of plasma etching (although the technology discussed here has also demonstrated application in other processes including deposition). The need to control the etch rates and etch profiles on a target substrate are of the most significant concern. Among the factors contributing to etch rate and etch depths are the ion energy distribution and the ion flux across the wafer. Capacitively coupled plasmas that use only one frequency cannot control both of these parameters simultaneously; rather independent control of both ion flux and energy requires a dual frequency CCP or other supplemental plasma source such as ECR or ICP. In plasma etching, it is important to have ions of sufficient energy bombard precisely controlled location and direction relative to the substrate being etched. Control of these ion characteristics is one of the leading research areas underway to advance these processes for future manufacturing flows. One way to do that is by establishing a method of controlling ion energy distributions where the flux, energy, and direction of travel of the ions can be controlled independently.

This thesis focuses on one method in particular to control these ion properties, which is to drive the sheath with two RF frequencies to control the wave pattern of ion energy distribution so that the high energy part of the wave is located precisely where desired.

This paper examines ion energy distribution when using two different frequencies to drive plasma where these frequencies are integer multiples of one another. By driving integer multiple frequencies (also called harmonics), the relative phase between the two frequency drives can be controlled. In this work, the impact of this phase locked waveform on ion energy properties is presented, starting with a theory on ion energy control using multi-frequency drive, extension of this theory to phase locked harmonic drive, and construction of an experimental apparatus that will enable validation of this model

Thesis Layout

This thesis lays out the theoretical work and diagnostic setup to demonstrate ion energy control using harmonic phase locked waveforms. In Part 1 a brief discussion on previous efforts to control and measure ion energy distributions is presented. Part 2 provides an overview of the sheath model used to demonstrate the capabilities of harmonic phase locked ion acceleration. Part 3 and Part 4 detail the experimental methods that would be employed to validate this model and present some preliminary data that demonstrates proper diagnostic functionality. Finally, in Part 5, a path for future work is presented along with conclusions made through the efforts detailed in Parts 1-4.

PART 1: Introduction

What is plasma and how does it form

There are four states of matter: solid, liquid, gas, and plasma. The first three we encounter and recognize constantly in daily activity. Plasma is equally present but less frequently noticed**.** The sun and every visible star is a fusion reactor of highly energetic plasma composed of mostly hydrogen, helium, and beryllium. Lightning is also plasma, comprising elements found in air. Both create plasma but by different means; the sun uses immense heat and gravitational confinement while lightning uses electrical potential. Mankind has leveraged plasmas for a variety of common applications as well. Fluorescent lighting, neon signs, and compact fluorescent light bulbs use plasmas to generate light. Vacuum tubes, the predecessor to the solid state circuit, used the diode like electrical properties of plasmas to give birth to the digital age.

To explain why large amounts of electricity or heat make plasma we must understand how atoms behave to form different materials in our everyday life. In construction, atoms may be described roughly as having a nucleus containing positively charged protons and neutral neutrons surrounded by one or more shells of electrons collectively having an equal negative charge. Charged particles with the same sign (that is positive or negative) repel one another, and particles of opposite charge attract. So in a hypothetical situation, two lone electrons will repel one another and want to move as far apart as possible (infinity). The same would happen with two protons. However, a proton and an electron will attract each other. The force that causes this to happen is called the Coulombic or electrical force. What prevents protons from crashing out of the nucleus to meet the electrons is a force even stronger than the electrical force: the “strong intervention” or the nuclear force. The nuclear force acts to bind protons and neutrons within the atomic nucleus. Atoms that are electrically neutral have an equal number of protons and electrons.

The state of matter can be determined by the amount of energy, or thermal motion, within the atomic particles. The particles in an atom are continually moving. Thermal energy is the amount of energy a substance possesses due to this motion. At very low temperatures, a given element will be a solid. As energy is added, the bond length changes because of thermal vibration between adjacent atoms in a solid structure and, as a result, weaken intermolecular bonds to other atoms, thereby changing the state of the element from solid to liquid to gas as the energy input increases.

If the energy becomes great enough, it can excite electrons to the point of exiting the respective orbitals of their nuclei. With the loss of an electron, the neutrally charged atom is converted into a positively charged ion. The process by which these electrons are liberated from neutral atoms is known as ionization. As the neutral atoms ionize into charged particles, the material becomes plasma, the fourth state of matter.

Ionization is the defining feature of plasma. The degree of ionization can vary from only a small fraction of the gas to nearly full ionization. Atoms with atomic numbers greater than one can experience multiple stages of ionization, losing multiple electrons to produce ions with strong positive charge. For the plasmas that will be discussed in this work, only single-ionized species tend to be present, and only one electron is stripped from the atoms through the ionization process. The presence of these unbound charged species creates a highly electrically conductive media that can respond to electromagnetic fields. This state is called the plasma state and on first order defines the fourth state of matter that exists in nature.

There are multiple ways to generate plasma; each method requires an energy input to both produce and maintain the rate of ionization need to sustain the plasma state. Man-made plasmas tend to utilize the application of an electric or magnetic field to accelerate the particles and control charge particle production and loss.

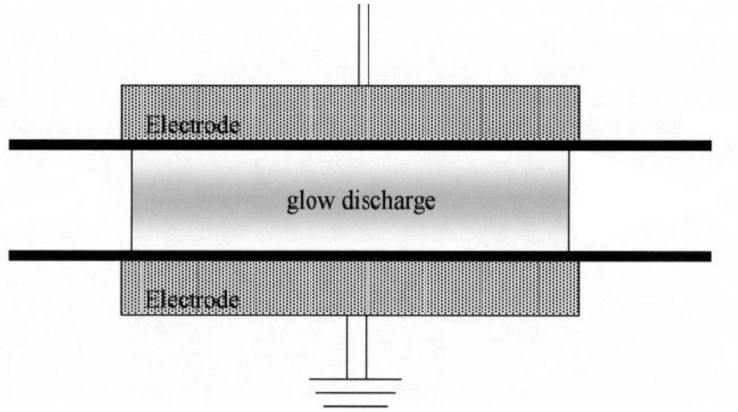

Figure 1 illustrates a simple example of how man-made plasmas are created.[1]

Plasmas and plasma sources are categorized based on their configuration and fundamental properties. The type of power source used to drive the system, typically categorized by frequency (DC, RF, microwave) is useful as each of these classes have fundamental differences in how they ignite and sustain a plasma. The pressure of the background gas, similarly, has significant influence on collective plasma behavior and heating modes, and plasma systems are typically broken up into low pressure, high pressure, and atmospheric due to these phenomena. The degree of ionization is also important, as it determines the dominant collision mechanisms in the plasma, and systems are classified as weakly, partially, or fully ionized. The temperature of the plasma components, both in magnitude and in relative value, is a strong identifier for the system set-up and the field of application for a plasma process, such as high temperature plasmas, thermal plasmas, low temperature plasmas, and non-equilibrium plasmas. The type of system used to induce a discharge (CCP, RIE, ICP, etc.) will dictate the type and degree of magnetization of the plasma particles, whether it be from the magnetization of both the ions and the electrons trapped in orbits, to partial with just the electrons trapped in the magnetic field, to non-magnetic, in which the magnetic field is too weak to trap any particles in orbit.

This paper will focus on the use of one or more independent RF power sources in a capacitively coupled configuration to produce hypothesized ion energy distribution results. The pressure range will be moderately low pressures ranging in the mTorr range, with a relatively low degree of ionization. The plasma is non-magnetized and does not have any trapped orbits or magnetic confinement of charged particles. The primary application for this configuration is industrial manufacturing processes, most notably plasma assisted manufacturing of electronic components. Plasmas in this configuration are typically very low temperature and the components of the plasma tend not to reside in thermal equilibrium with themselves or with each other, having characteristically non-Maxwellian temperature distributions for charged particles (namely electrons) and average temperatures for electrons, ions, and gas species that can vary by orders of magnitude. Specifically, these plasmas tend to have ion and gas temperatures in the vicinity of room temperature (300K – 500K) and electron temperatures closer to 5eV (approximately 60,000K).

A simple method of producing artificial plasma is to introduce an inert gas into a chamber containing parallel electrodes on either side of the chamber and then supply a power source to strike the gas between the two plates. The plasma is initiated by the electric field induced between the plates and maintained primarily through simple ohmic heating of the electrons, similar to the heating mechanisms seen in lossy dielectric capacitors. As the incoming energy ionizes some of the atoms, the lighter, more mobile electrons will travel swiftly, colliding with other atoms. Typically, the first collision between an electron and an atom produces one ion and two electrons. In a short period of time, an avalanche effect results and the number of charged particles increases hugely. This process continues as long as the electrical potential is maintained.

In a simple model, the plasma develops into two parts, the thin sheath areas next to the electrodes and walls of the chamber and the bulk plasma in between. Plasmas are normally quasi-neutral, that is, the net positive charge is about equal to the net negative charge. However, in the configuration described here, the lighter, hotter electrons respond on a much faster timescale than the heavier, cooler ions. At very short timescales, this difference in particle mobility results in a rapid loss of negative charge to the walls at the periphery of the plasma over a short enough timescale that the ions cannot respond. The low electron density results in an excess positive charge at the periphery of the plasma. This region of positive charge generates the sheath at the plasma boundary. Sheaths are also known as dark spaces due to the absence of luminosity associated with the bulk plasma.

The color taken on by plasma is determined by the specific gas composition that is subsequently excited through electron impact. The light emitted from plasma is caused by returning excited electrons to their ground state (their original position before being excited). The color of the light is different for every different gas species because each atom or molecular species has unique quantum transitions. Each element has well defined energies between the electron states and thus each gas emits a specific wavelength of light during this excitation and de-excitation process. For example, as seen in Figure (2), argon plasma emits purple light, nitrogen emits a reddish orange light, fluorocarbon emits blue, and oxygen emits a pale white.

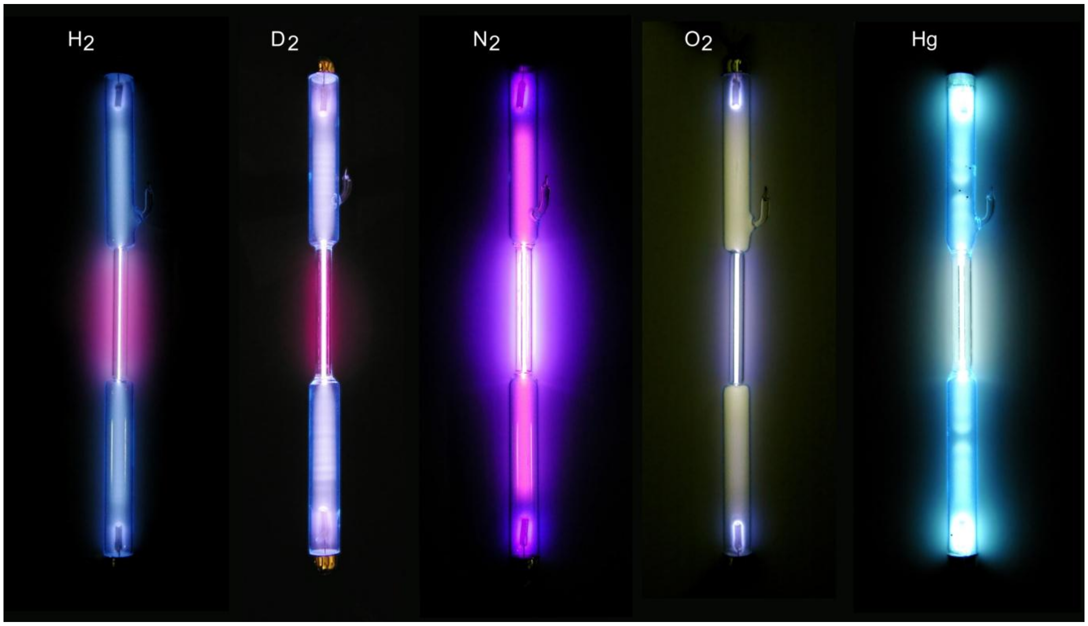

Figure 2: Plasma discharge color emitted from hydrogen, deuterium, nitrogen, oxygen, and mercury, as seen from left to right.[2]

The frequencies at which the voltage is applied in a typical capacitive RF discharge can range from 10’s of kHz to 100’s of MHz. Within this range the ions in the bulk plasma, which are far more massive than the electrons, are negligibly affected by the oscillating electric fields. Electrons on the other hand, gain considerable energy as they are light enough to be accelerated by the oscillating field. Energy levels are mainly determined by particle balance of the system. It is measured using an array of diagnostics including Thompson Scattering and Langmuir probe electrical characteristics.

The chamber and the electrodes are made of metal and, as the electrons collide with them, they develop a negative charge that repels subsequent electrons, thus allowing the plasma to retain a neutral net charge. This net neutrality is maintained because as the boundaries of the plasma become negatively charged, they attract a small amount of the positively charged ions. A user can manipulate input power, chamber pressure, gas flow rate, gas composition, plate separation, and geometry within the process chamber, but ultimately the magnitude of the electric and magnetic fields will be determined by conservation of flux and maintaining quasi-neutrality of the plasma by balancing electron and ion loss so that they remain equal. The reasoning guiding this theory further discussed at the beginning or Part 2.

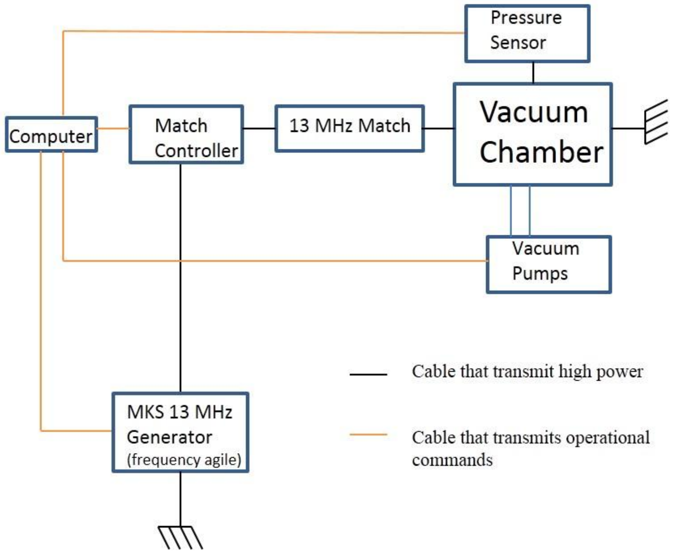

Figure 3 depicts a simplified system.

The remaining parameters mentioned above can be easily altered between process runs and even during the process itself from a computer or other controller devices, as Figure (3) indicates. The simplest parameter to understand is how much power the electrode receives. An increase in power increases both the density and the energy of the free electrons; thus the DC voltage becomes more negative. The pressure does not have a linear effect on the plasma, however. Ultimately, the DC bias voltage becomes less negative with increasing pressure.[3]

Common Techniques and History

Three common methods used in the commercial semiconductor industry today are:

(i) CCP – Capacitively Coupled Plasma
(ii) ICP – Inductively Coupled Plasma
(iii) ECR – Electron Cyclotron Resonance Plasma

As previously mentioned, all the common techniques for generating plasma have a capacitive coupling element to them. ICPs primarily stimulate magnetic fields but have corresponding electric fields that are relatively low. The electric fields in an inductive discharge represent an inductive component.[4] Even when an inductive source generates plasma it is also active in a capacitive mode that presents some capacitive coupling which is responsible for oscillations in the plasma potential.[5] It is these oscillations that accelerate the ions in the sheath. This is sometimes an undesirable effect since the extra energy gained by the ions can contaminate the substrate surface because they cause heating and sputtering of the dielectric window.[6] This is often remedied by placing a faraday screen between the inductive coil and the dielectric window. By aligning the conducting wires of the screen perpendicular to the direction of current through the coils, the E-mode field can be screened while allowing the H-Mode that promotes inductive coupling to pass through. However, since the H-Mode cannot ignite a plasma on its own, this configuration requires additional systems for initiation of the plasma discharge.

Capacitively coupled plasmas consist of two plates that are in parallel; the applied RF field generates a potential drop created between the electrodes, providing an accelerating path for ohmic and stochastic heating of electrons. This is the most common technique to strike and sustain a plasma. However, limitations exist primarily due to the strong accelerating field perpendicular to the electrodes in the sheath region that dissipate up to 90% of the absorbed RF power through ion acceleration, making plasmas with significant ion energy composition and relatively low electron densities. This is often remedied through intelligent selection of RF frequency for power delivery; as frequency increases the sheath reactance (and subsequent voltage drop) is reduced, allowing for more power coupling for electron ion pair production and less for ion energy. However, the coupling of the two parameters still exists for single frequency operation.

Electron cyclotron resonance plasmas utilize a microwave field that resonates with electrons orbiting a static magnetic field. In this way the electrons gain energy during their periodic cycling and their energy is proportional to the time between collisions.[7] This technique is only suitable for etching that requires little penetration of the substrate surface. There are several systems with very uniform ECR applications that are often used in combination with a biased electrode for ion acceleration control. Their low pressure operation allows for the desired species to diffuse all the way down to the wafer.

For industrial purposes, it is necessary to know how plasma density, sheath width, potential drop, and corresponding IEDs change with the increase of low-frequency voltage in a dual frequency rf system.[8] An increase in low-frequency voltage leads to a decrease in plasma density with a subsequent increase of the sheath width. The low frequency controls the ion energy (which is an important factor in etching processes), while the high frequency independently controls the ion flux (which determines the etch rate).

PART 2: Theory and Model of Capacitively Coupled Discharges

Ion Transit Time and Single Frequency Theory

In order to understand the effects of two frequencies on the distribution of ion energies that pass through an RF driven sheath, we first consider how ion energy distributions behave when using only one frequency. In a collisionless sheath (one in which the sheath width is much smaller than the ion mean free path and thus minimizing the space at which an angular collision can occur) the transit time is the primary factor that determines the shape of the ion energy distribution. This factor is the time taken for an ion to cross from one side of the sheath to the other when the sheath drop is at its DC value.

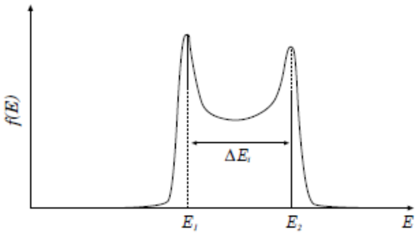

Figure 4: The two peaks in the distribution correspond to the minimum and maximum sheath drops, or rather where the voltage change occurs most slowly.[9]

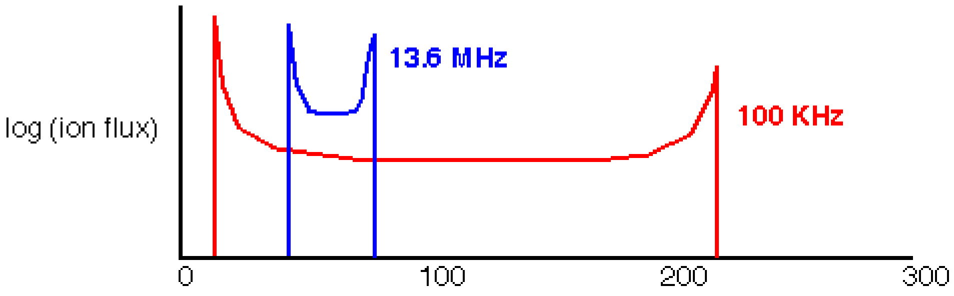

Figure 5 illustrates how higher frequencies produce more narrow ion energies than low frequencies.[10]

At low frequencies ions will have a very small transit time compared to the RF cycle and thus respond to the instantaneous sheath voltage. However, at high frequencies, it takes multiple RF cycles for ions to traverse the sheath and the ions cannot respond to the instantaneous sheath voltage. Instead, at high frequencies, the ions only respond to the average sheath voltage. The energy distribution of high frequency results in a narrower distribution than a low frequency regime creates, as illustrated in Figure (5). At low frequencies, the ion energy distribution depends on what the instantaneous phase of the RF cycle is when each ion enters, thus resulting in a wide distribution of ion energy.

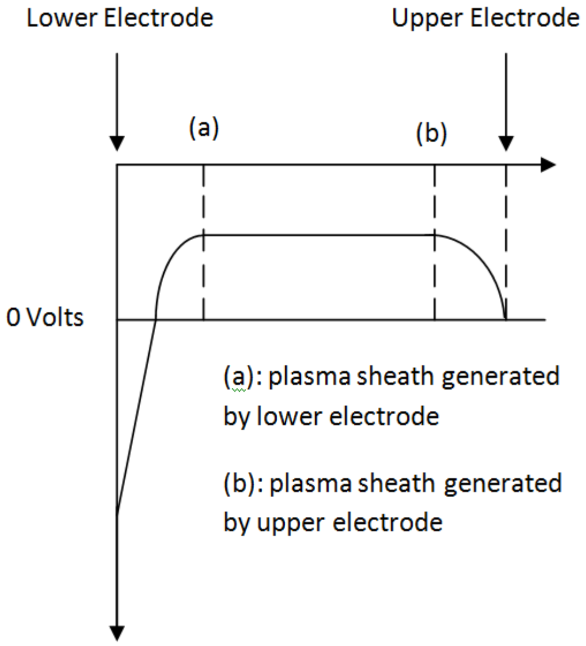

Figure 6 shows how voltage varies between the lower and upper electrodes.[11]

When operating with only one frequency in a CCP, the ion energy distribution on a substrate is directly related to the ratio between the ion transit time and the RF cycle period. This ratio in turn is governed by the RF frequency, sheath width, and sheath voltage drop.

As voltage increases the structure of the peaks in an IEDF become more prominent. The number of peaks in a distribution using dual frequency is determined by which harmonic of the low frequency is being used. Increasing frequency reduces the overall width (edges at minimum and maximum) of the distribution. Altering the phase moves the placement of the peaks but does not affect the number of peaks or the maximum or minimum sheath voltages. This is visually expanded upon at the end of Part 2 in Figures (15), (16), and (17).

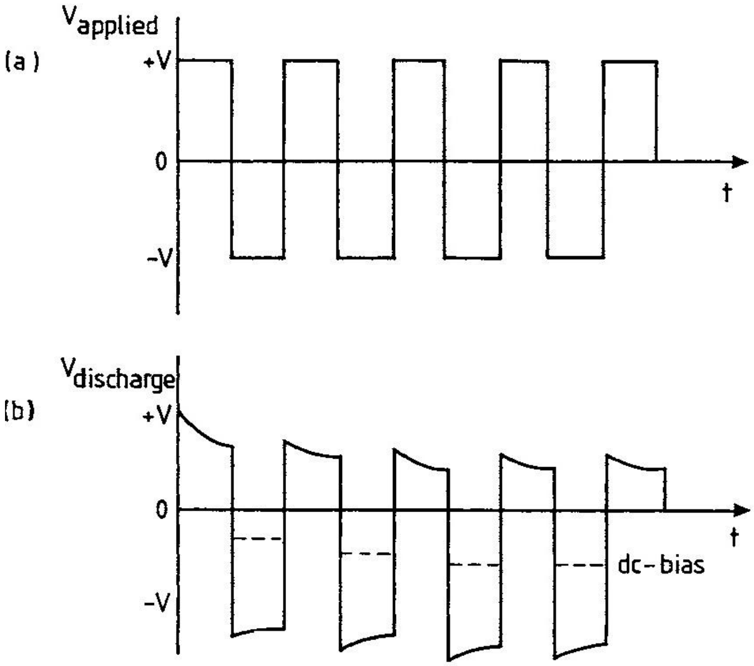

Figure 7. Development of self-bias or DC bias in a CCP in the simplified case of a rectangular pulse: (a) applied voltage; and (b) resulting voltage over the discharge as a function of time, and resulting dc-bias, indicated by the dashed line.[1]

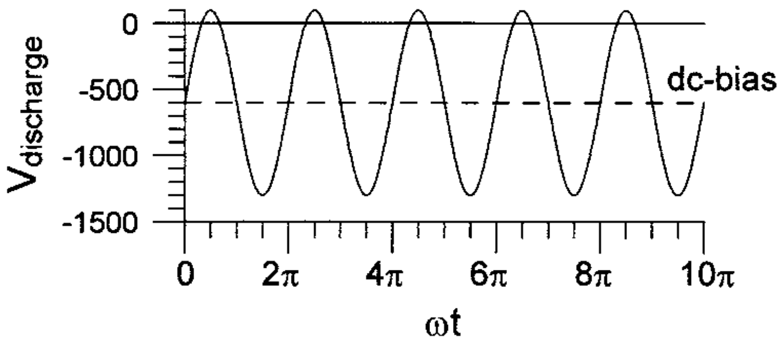

Figure 8: Shows a typical sinusoidal voltage in a rf CCP in the case of a large, negative DC bias. The solid line represents the voltage between both electrodes, and the dashed line shows the resulting DC bias at the rf powered electrode.[1]

Dual Frequency Ion Energy Theory

Multi-frequency RF power delivery for IEDF control is commonplace in semiconductor manufacturing, particularly in plasma etch applications.[5] Recently, two frequency drives at which the higher drive frequency is a harmonic of the lower drive frequency has shown influence on IEDF's with phase acting as an additional tuning knob for control.[12] In this work, an RF sheath model that assumes a matrix sheath condition and known electron density is used to compare the influence of multiple frequencies over transient sheath parameters, specifically the time dependent potential across the powered sheath.

The desired frequencies are 13.56MHz and its first harmonic, 27MHz. IEDF's are obtained for conditions where the two frequencies are integer multiples of each other and compared to the more typical case where the frequencies are not integers of each other. The comparison in this work will be from 2MHz and 13MHz.[5] In either case the low frequency affects the sheath and the high frequency affects the bulk plasma. Frequency mixing flattens the low voltage distribution of the sheath potential. Control of the distribution width is identical with respect to relative RF current from two sources for both the integer and non-integer cases. The integer frequency drive produces (n-1) intermediate peaks in the distribution between the maximum and minimum energies whose energy and magnitude can be controlled with the relative phase of the two waveforms.

Manipulation of the phase and amplitude of these two power sources can also produce some unique distribution functions. The model used to test this theory assumes that both the high and low frequencies have equal percent contributions, which combine to create the “mixed frequency.” This frequency’s composition is determined by phase, or rather the allowed constructive or destructive interference the low and high frequencies create upon mixing.

Prior Work and IED Model

The IEDF plays an integral role in etching and deposition techniques on silicon wafers and chip manufacturing. High-energy ions increases etch rates far superior than those of a linear combination of single-peak IEDF. The voltage drop in a sheath adjacent to the substrate determines ion energy in low-pressure discharges, with the sheath voltage controlled by the applied RF bias. Ions are then accelerated by the electric field in the sheath region, and in the absence of collision, strike the substrate.[13,14] Figure (9) illustrates etch rate dependence on ion energy. By controlling the shape of the IEDF via altering the input parameters such as voltage, current, and phase, a variable width can be produced. Increasing the integer frequency drive, *n*, adds to the number of peaks seen in a distribution. An increase in frequency decreases the overall width, just as a decrease in frequency widens the overall distribution width. Knowing each frequency component of the sheath potential allows a derivation for an ion apparent potential. Frequency mixing introduces an inter-modulation component that flattens the low-voltage portion of the time-varying sheath potential, thus producing a low-energy skew in the IEDF, as Figure (10) demonstrates. Previous researchers compiled voltage amplitudes for principal frequency and ion apparent potentials for principal frequency components of a dual frequency rf sheath.[5]

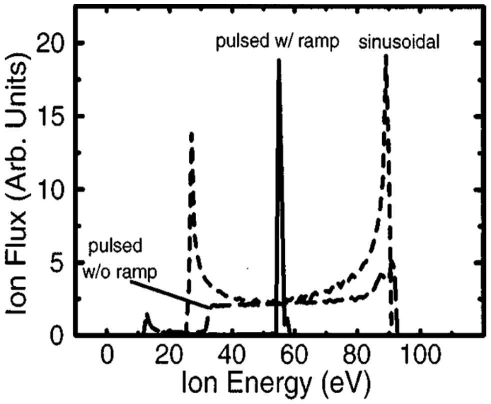

Figure 9, etch rate due to ion flux versus ion energy.[15]

Peak currents are determined by single frequency current to generate a given DC potential. Set up a base frequency *f*, which $= \frac{\omega}{2\pi}$, and a high frequency harmonic defined by *n*-*f* and a phase component.

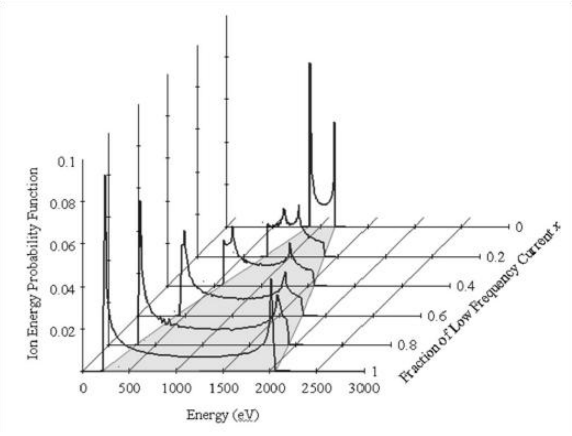

Figure 10 shows that IEDF width decreases with increase in high frequency contribution. Also the inter-modulation component flattens a portion of the time-varying sheath, producing a low-energy skew in the IEDF.[16]

The etch profile of a given substrate narrows as it deepens, as Figure (11) recreates a side view of such an etch. The box diagram shown in Figure (12) illustrates the electrical set up of the system used for this model.

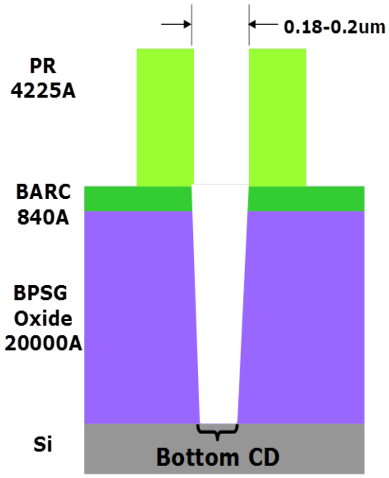

Figure 11 is a computer generated image of what a vertical slice of an etch would look life for a silicon wafer.[17]

The ions see a damped potential in the sheath where the magnitude of the oscillation is damped by a term in the denominator.[3,18] The sheath voltage needs to be broken up into frequency components to capture this for multiple frequencies.

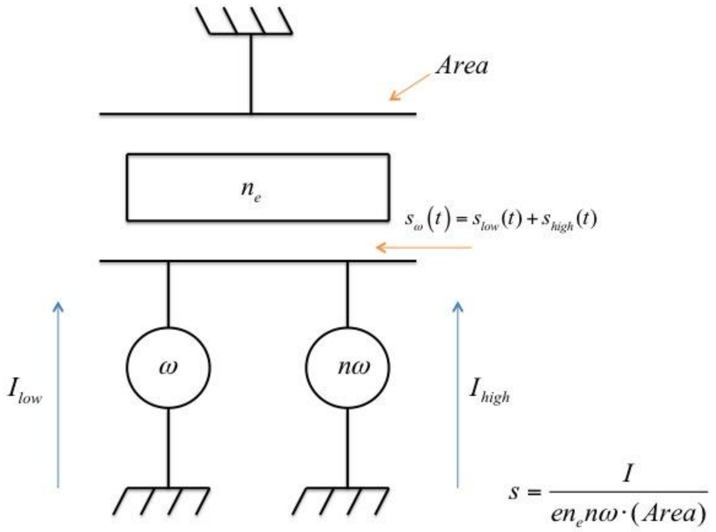

Figure 12: The mixed dual frequency CCP, with one electrode powered and the other remains grounded.

The IEDF calculation is done in full in Appendix A, but an explanation of the steps are detailed as follows:

IEDF Calculation Overview

Example Discharge using Argon gas.

RF Drive Set points: fraction of low frequency power over high frequency power is x. So an x value of 1 is when there is no power contribution from the higher frequency generator. Set up a base frequency f, a high frequency harmonic defined by $n \cdot f$, and a phase component φ.

Peak currents are determined by single frequency current to generate a given DC potential:

$$I_{low} = x\sqrt{-8\pi^2 V_{dc}\varepsilon_0 e n_e f^2 Area^2} \tag{1}$$

$$I_{high} = (1-x)\sqrt{-8\pi^2 V_{dc}\varepsilon_0 en_e (nf)^2 \; Area^2} \tag{2}$$

These can be rewritten as:

$$I_{low} = x\frac{Area(2\pi f)}{3}\sqrt{-6\cdot 2V_{dc}\varepsilon_0 en_e} \tag{3}$$

$$I_{high} = (1-x)\frac{Area(2\pi nf)}{3}\sqrt{-6\cdot 2V_{dc}\varepsilon_0 en_e} \tag{4}$$

The next step is to determine the sheath widths based on the high and low current, remembering that the "high" relationship always refers to the multiplication of the drive frequency by the chosen harmonic value, *n*. The time-averaged sheath thickness, S_0, is the sum of the low and high components of the sheath amplitude, and *S(t)* is the time-varying oscillation of a single sheath driven by both high and low frequencies.

$$s_{low} = \frac{I_{low}}{en_e 2\pi f\,(Area)} \tag{5}$$

$$s_{high} = \frac{I_{high}}{en_e 2\pi nf\,(Area)} \tag{6}$$

$$s_0 = s_{low} + s_{high} \tag{7}$$

$$s(t) = s_{low} + s_{high} + s_{low}\sin(2\pi ft) + s_{high}\sin(2\pi nft + \varphi) \tag{8}$$

The transit time for an ion across the sheath is defined by τ_i.

$$\tau_i = 3s_0\sqrt{\frac{m_i}{2eV_{dc}}} \tag{9}$$

By substituting equation (8) into equation (10) the sheath potential for the system can be calculated by treating it as a parallel plate vacuum capacitor holding a charge of $en_e/2$ with a time-varying gap equal to S_0, resulting in Equation (11). Purely as a means to shorten the lengths of the equations, Equations (12) is defined and subsequently the sheath potential is rewritten in Equation (13).**16**

Sheath potential:

$$V_{sheath}\left(t\right)=-\frac{en_e}{2\varepsilon_0}s\left(t\right)^2 \tag{10}$$

$$V_{sheath}\left(t\right)=-\frac{en_e}{2\varepsilon_0}\left[s_{low}+s_{high}+s_{low}\sin\left(2\pi ft\right)+s_{high}\sin\left(2\pi nft+\varphi\right)\right]^2 \tag{11}$$

$$\omega=2\pi f \tag{12}$$

$$V_{sheath}\left(t\right)=-\frac{en_e}{2\varepsilon_0}\left[s_{low}+s_{high}+s_{low}\sin\left(\omega t\right)+s_{high}\sin\left(n\omega t+\varphi\right)\right]^2 \tag{13}$$

The ions see a damped potential in the sheath where the magnitude of the oscillation is damped by:

Knowing each frequency component of the sheath potential allows for the derivation of an ion apparent potential, where the amplitude of each frequency is damped or weighted by a $1/\omega\tau_i$ term. The sheath voltage needs to be broken up into frequency components to capture this for multiple frequencies. Equation (14) displays the squared out expression inside the brackets from Equation (13).

$$\begin{gathered}\left(s_{low}+s_{high}\right)^2+2\left(s_{low}+s_{high}\right)s_{low}\sin\left(\omega t\right)+2s_{high}\left(s_{low}+s_{high}\right)\sin\left(n\omega t+\varphi\right)+s_{low}^2\sin^2\left(\omega t\right)+\\ 2s_{low}s_{high}\sin\left(n\omega t+\varphi\right)\sin\left(\omega t\right)+s_{high}^2\sin^2\left(n\omega t+\varphi\right)\end{gathered} \tag{14}$$

Using double angle trigonometric identities from Equations (15) and (16), the fully expanded expression from Equation (13) can be solved. This is expressed in Equation (17).

$$\sin^2(\omega t) \equiv \frac{1}{2} - \frac{\cos(2\omega t)}{2} \qquad \sin^2(n\omega t + \varphi) \equiv \frac{1}{2} - \frac{\cos(2n\omega t + 2\varphi)}{2} \tag{15}$$

$$\sin(n\omega t + \varphi)\sin(\omega t) \equiv \frac{1}{2}\left\{\cos\left[\omega t(n-1) + \varphi\right] - \cos\left[\omega t(n+1) + \varphi\right]\right\} \tag{16}$$

$$\begin{gathered}\left(s_{low} + s_{high}\right)^2 + 2\left(s_{low} + s_{high}\right)s_{low}\sin(\omega t) + 2s_{high}\left(s_{low} + s_{high}\right)\sin(n\omega t + \varphi) + s_{low}^2\left(\frac{1}{2} - \frac{\cos(2\omega t)}{2}\right) + \\ 2s_{low}s_{high}\frac{1}{2}\left\{\cos\left[\omega t(n-1) + \varphi\right] - \cos\left[\omega t(n+1) + \varphi\right]\right\} + s_{high}^2\left(\frac{1}{2} - \frac{\cos(2n\omega t + 2\varphi)}{2}\right)\end{gathered} \tag{17}$$

The multiple components of the frequency are broken down into four categories: DC, Fundamental, Harmonic, and Mixing.

DC Component:

$$\frac{3}{2}s_{low}^2 + \frac{3}{2}s_{high}^2 + 2s_{low}s_{high} \tag{18}$$

Fundamental Component:

$$2s_{low}\left(s_{low} + s_{high}\right)\sin(\omega t) + 2s_{high}\left(s_{low} + s_{high}\right)\sin(n\omega t + \varphi) \tag{19}$$

Harmonic Component:

$$-\frac{1}{2}s_{low}^2\cos(2\omega t) - \frac{1}{2}s_{high}^2\cos(2n\omega t + 2\varphi) \tag{20}$$

Mixing Component:

$$s_{low}s_{high}\left\{\cos\left[\omega t(n-1) + \varphi\right] - \cos\left[\omega t(n+1) + \varphi\right]\right\} \tag{21}$$

By combining these four components the time-varying sheath voltage is established in Equation (22):

$$V_{sheath}\left(t\right)=-\frac{en_e}{2\varepsilon_0}\left[\begin{array}{l}\frac{3}{2}s_{low}^2+\frac{3}{2}s_{high}^2+2s_{low}s_{high}+2s_{low}\left(s_{low}+s_{high}\right)\sin\left(\omega t\right)+2s_{high}\left(s_{low}+s_{high}\right)\sin\left(n\omega t+\varphi\right)\\-\frac{1}{2}s_{low}^2\cos\left(2\omega t\right)-\frac{1}{2}s_{high}^2\cos\left(2n\omega t+2\varphi\right)+s_{low}s_{high}\left\{\cos\left[\omega t\left(n-1\right)+\varphi\right]-\cos\left[\omega t\left(n+1\right)+\varphi\right]\right\}\end{array}\right] \tag{22}$$

The voltage that the ion sees is damped by the $1/\omega\tau_i$ term. Each frequency component with a phase influence needs to be damped to that component's frequency. The full time-varying ion potential is expressed in Equation (23).

$$V_{ion}\left(t\right)=-\frac{en_e}{2\varepsilon_0}\left[\begin{array}{l}\frac{3}{2}s_{low}^2+\frac{3}{2}s_{high}^2+2s_{low}s_{high}+\frac{2s_{low}\left(s_{low}+s_{high}\right)}{\omega\tau_i}\sin\left(\omega t\right)+\frac{2s_{high}\left(s_{low}+s_{high}\right)}{\omega n\tau_i}\sin\left(n\omega t+\varphi\right)\\-\frac{1}{2}\frac{s_{low}^2}{4\omega\tau_i}\cos\left(2\omega t\right)-\frac{1}{2}\frac{s_{high}^2}{4n\omega\tau_i}\cos\left(2n\omega t+2\varphi\right)+\frac{s_{low}s_{high}}{\omega\left(n-1\right)\tau_i}\cos\left[\omega t\left(n-1\right)+\varphi\right]-\frac{s_{low}s_{high}}{\omega\left(n+1\right)\tau_i}\cos\left[\omega t\left(n+1\right)+\varphi\right]\end{array}\right] \tag{23}$$

A sample set of conditions using this model can determine the ion apparent voltage as it oscillates with the sheath, as well as produce an approximate ion energy distribution. To do this, use sample plasma conditions of:

$n_e = 2.46 \cdot 10^9\ cm^{-3}$ $V_{dc} = -70\ Volts$ $m_i = 40 \cdot 1.67 \cdot 10^{-27}\ kg$

$Area = \pi \cdot (75\ mm)^2$ $f = 13.56\ MHz$ $x = 0.5$ $\varphi = 45°$ $n = 2$

The oscillation of the sheath as it tracks with the ion apparent voltage is displayed in Figure (13), and the IEDF for these specific parameters is shown in Figure (14).

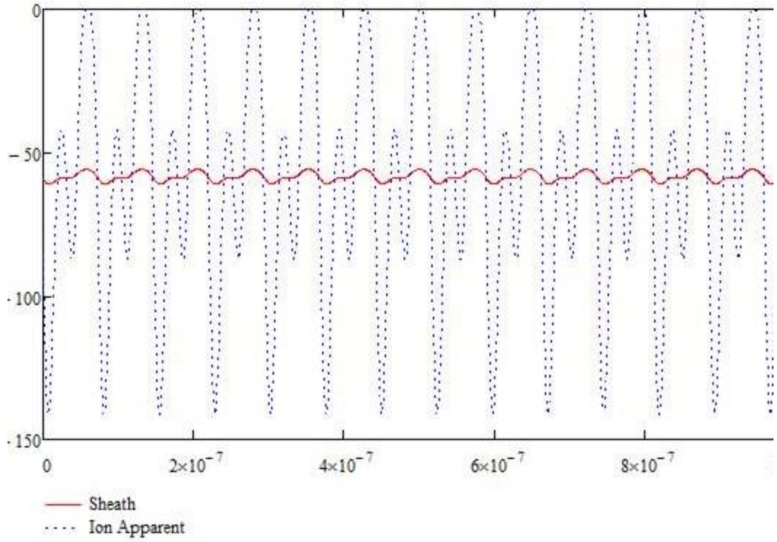

Figure 13. Ion apparent and sheath voltages.

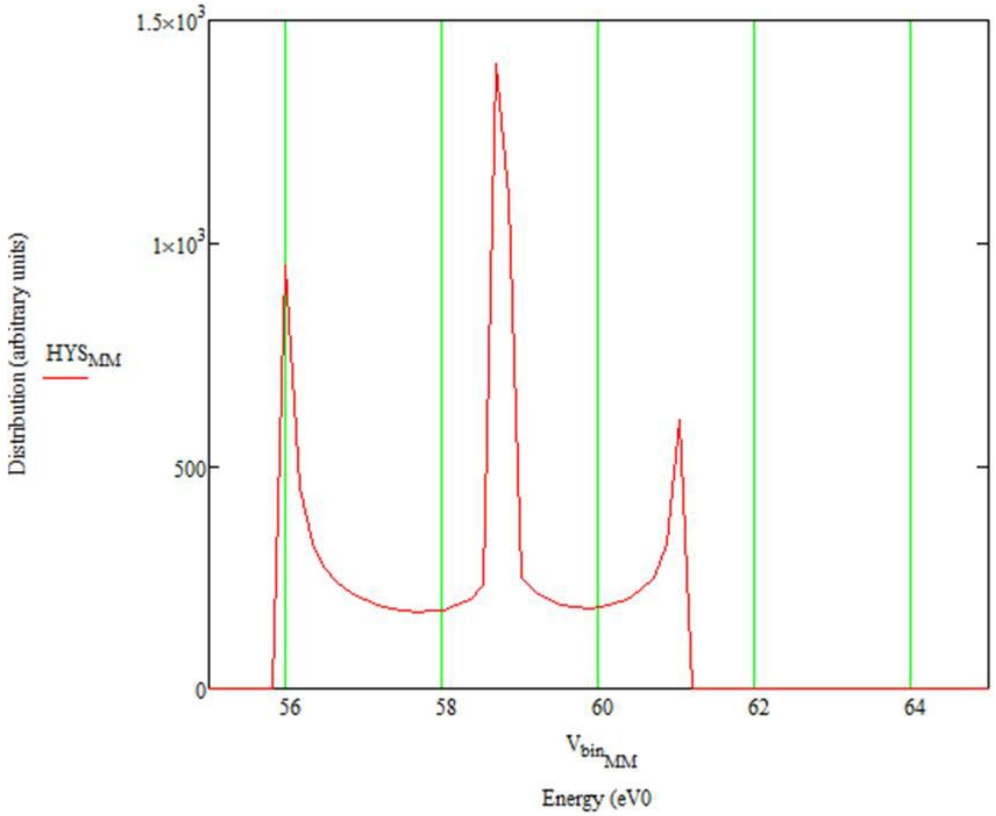

Figure 14. IEDF output from MathCad using model and sample conditions.

Harmonic Effect, Current Ratio Effect, and Phase Effect

The model and the data should indicate that increasing the number of harmonics, *n*, calculated while drive frequency and phase stay constant only adds to the number of peaks in the distribution, called the harmonic effect, and is demonstrated in Figure (15).

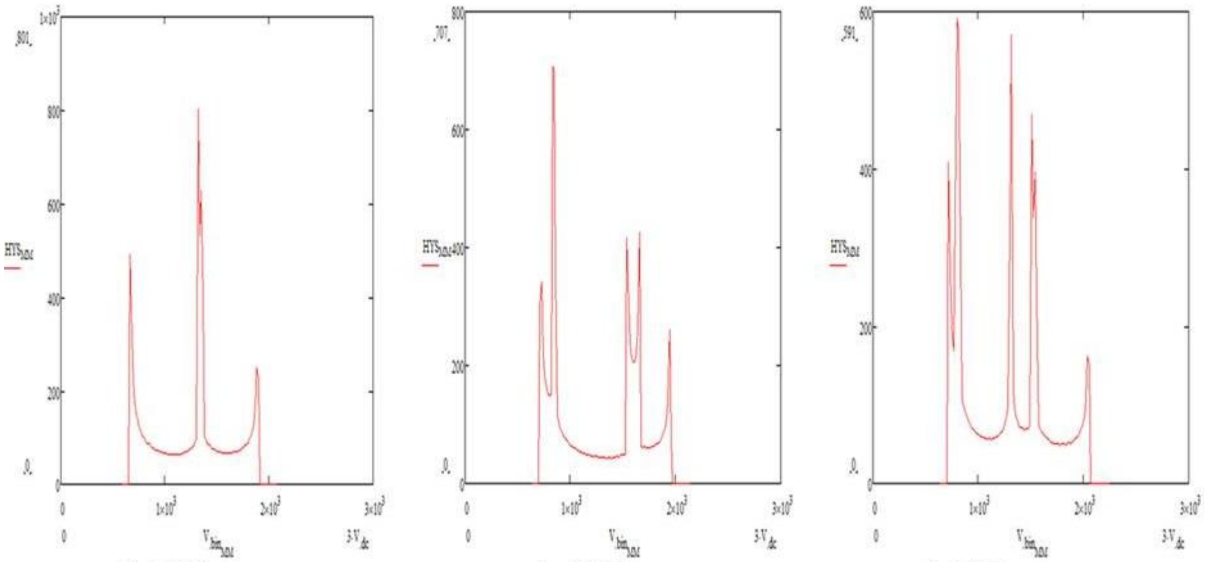

f = 2 MHz
phase = 45°
n = 2

f = 2 MHz
phase = 45°
n = 3

f = 2 MHz
phase = 45°
n = 4

Figure 15 indicates that adjusting *n* does not affect the width of the ion energy distribution.

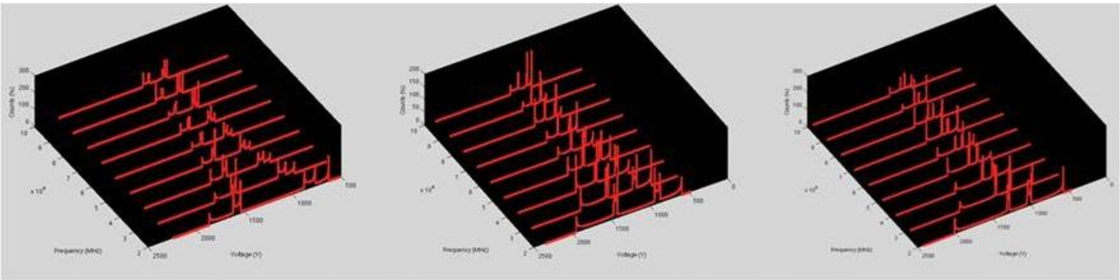

n = 3
phase = 45 degrees

n = 3
phase = 90 degrees

n = 3
phase = 135 degrees

Figure 16 displays three plots that have a fixed number of harmonics, drive frequency (between 2 MHz and 10 MHz), and relative current, but three different phase interference contributions.

Increasing the drive frequency decreases the overall width of the distribution. Figure (16) illustrates this as well as the current ratio effect, which states that the width of the distribution still depends on frequency selection, harmonic selection, and relative current. The phase effect illustrates that as phase shifts between zero degrees and 360 degrees, the total energy at a given peak does not change, but rather the peak distribution moves across the entire voltage range, as seen in Figure (17).

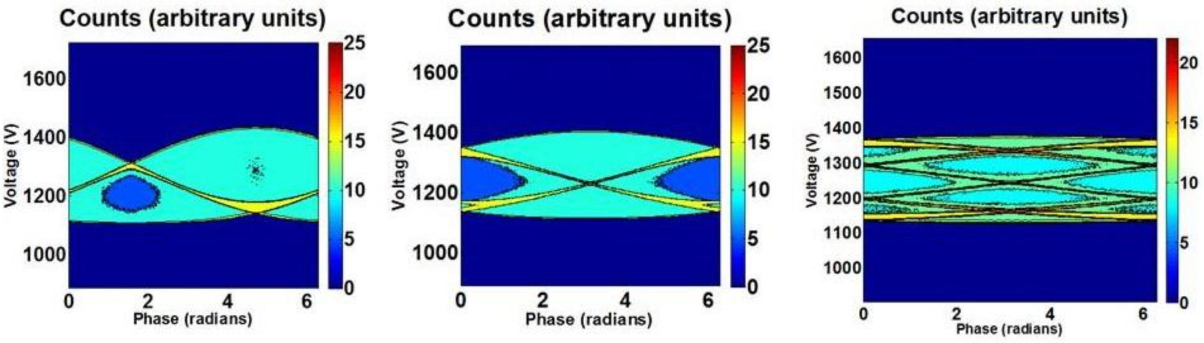

$n = 2$ $n = 3$ $n = 7$

Figure 17 demonstrates how altering phase allows peaks to track over the entire voltage range.

Notice that distributions with two or more harmonics in play that there are identifiable points at which constructive interference of the two frequencies causes a spike in ion energy as the peaks pass over one another.

Comparison of Single, Dual, and Phase-locked Frequency Discharges

Radio frequency capacitively coupled plasma discharges are still a developing field and each technique has its own benefits and detractors. Single frequency discharges, as is used in the data collection section of this thesis can used to obtain two peaks in their IED and to calculate the average ion energy. Dual frequency plasmas can attain these same specs but also allow for width control of the maximum and minimum ion energies. Dual frequency phase-locking when only concerned with using the first harmonic of the drive frequency allows for three peaks in the IED and determination of the average energy of the ions between a set maximum and minimum voltage. However, by specifying the phase, the position of the peaks may be moved across the full range from minimum to maximum. This is not possible when using dual frequency phase-locked discharges with more than the first harmonic. Each additional harmonic adds a peak, and as seen in Figure (17), when n=3 or n=7, the peaks can only skew between minimum and maximum by interfering with other ion energy peaks. Table (1) further illustrates these distinctions. Note that none of the techniques are able to determine information about collisions, as they all require collisionless sheaths as an initial condition.

Table 1: Capabilities of various types of rf discharges.

	Single	Dual	Phase (n=2)	Phase (n>2)
Avg. Energy	X	X	X	X
Width Control	--	X	--	X
Peaks	2	2	3	3 + n
Skew	--	--	X	--
Collisions	--	--	--	--

PART 3: Experimental Set-Up

In the laboratory the electrons are usually excited by an alternating current voltage in tune with a 13.56 MHz radio frequency generator. The matching network can either have a tuning mechanism built in or can be supplied one externally, as is the case in the apparatus used herein. Pressure is regulated by strong vacuum pumps, usually named “turbo pumps,” in conjunction with a “throttle valve.” This valve can rotate between closed, at which point a flange is horizontal across the turbo pump airflow entrance allowing no further reduction of pressure, or open, which is when the valve has rotated 90 degrees to allow full vacuum pumping. A specific gas composition is located inside the vacuum chamber, some of which is now flowing between the two electrodes waiting to be ignited by an electric potential drop between them.

Constructional Design

For this paper, all of the experimental work was conducted using the following apparatus and parameter descriptions. The process chamber is made of stainless steel and has an approximate volume of 30 liters. Argon gas flows between two parallel and equally sized electrodes, one of which is powered by a Huttinger Electronic's PFG 300 watt RF generator, and tuned with a RFPP 13.56 MHz matching network. While most theory and data collection for this experiment is only concerned with 13.56 MHz as the driving frequency, some comparisons to 60 MHz rf power are also measured, using an Advanced Energy generator and its companion RF Navigator matching network. To achieve the greatest precision about the exact voltage and current that will travel through the transmission lines prior to powering the electrodes, a custom probe and probe analyzer (which is calibrated to the specific probe being used) designed by M.K.S. has been added to the system between the Matching Network and the transmission lines running to the electrodes. The pressure in the chamber is monitored by an M.K.S. Baratron (1 mTorr – 1 Torr), which relays its' readouts to the M.K.S. Pressure Controller. The pressure controller mediates the pressure reading from the Baratron and properly aligns the throttle valve to the desired pressure after the gas flow has been set using the mass flow controller (MFC). Extra valves, all of which are manually controlled, exist between the pumps to allow for maintenance to different parts of the system without needing to fully vent the chamber. The electrical analysis of the system is performed by a Langmuir probe which sits in the center of the discharge, and a retarding field energy analyzer (RFEA) can be placed on either electrode depending on desired sheath precision. The former ascertains details about the electrons and the latter determines characteristics of the ions, respectively. Both probes are made by Impedans. The sheath on the side of the powered electrode is substantially larger than on the grounded electrode; therefore, more precise IEDs are measured when the probe is attached to the grounded electrode as there are fewer ion collisions in the sheath.

The two primary tools used are the Langmuir probe and the RFEA probe, and thus it is important to briefly explain the internal operation of each. A Langmuir probe belongs to a group of invasive plasma diagnostics, and is comprised of a thin wire electrode that is situated in the center of the bulk plasma region. Voltage is applied between the wire and a grounded electrode, and voltage is scanned within a certain region (chosen automatically or by the user, if desired). The resulting voltage/current (V/I) trace determines characteristics such as plasma potential V_p, mean electron temperature T_e, electron density n_e, and floating potential.

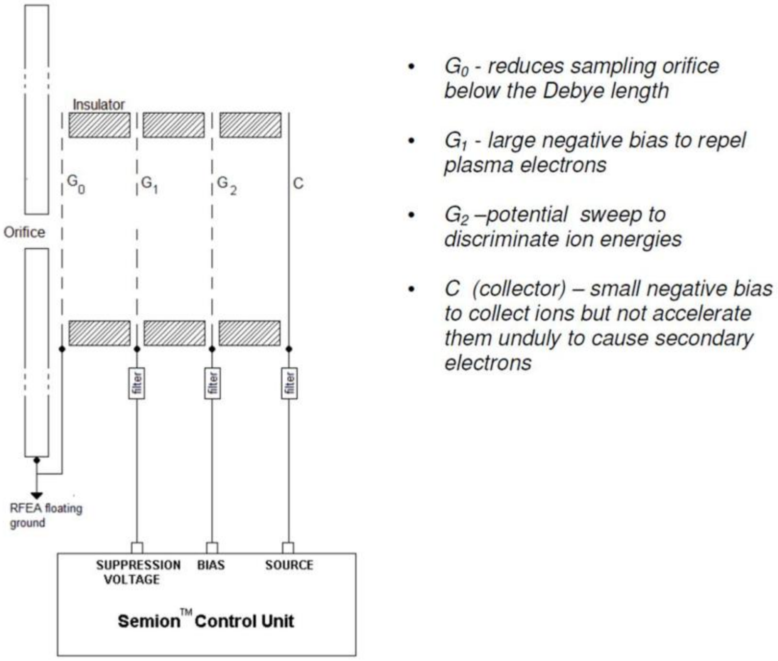

- *G_0 - reduces sampling orifice below the Debye length*
- *G_1 - large negative bias to repel plasma electrons*
- *G_2 –potential sweep to discriminate ion energies*
- *C (collector) – small negative bias to collect ions but not accelerate them unduly to cause secondary electrons*

Figure 18. Diagram of how the RFEA sensor is connected to the voltage outputs of the Semion Control Unit (SCU) as depicted in the user manual.[19]

The Retarding field energy analyzer (RFEA), considered a non-invasive tool, is essentially an electrostatic probe which applies negative DC voltages across its aluminum disc-shaped surface to attract ions while repelling electrons. The disc area of the probe lays flush against the grounded electrode such that incoming ions bombard the face of the probe at any angle perpendicular to its surface. The Semion 800 used in this experiment has a button probe that measures 33mm in diameter, a holder diameter of 70mm, and a thickness of 5mm. Ions enter the RFEA through a sampling aperture exposed to the plasma. A grid, shown in Figure (18), in a plane perpendicular to the direction of ion travel, is biased with a potential sweep, creating a potential barrier for the charged plasma species of interest. A detector plate oriented parallel to the grid collects the current of charged particles with sufficient energy to cross the potential barrier. The calculated IED is the energy distribution of the ions perpendicular to the electrode surface from the resultant current-voltage characteristic.[20]

Chamber Design and Equipment Layout

Inside the chamber the electrodes connect to hollow, vacuum sealed pipes that link the transmission lines from the matching network outside the chamber to the back of the electrode inside the chamber. Each pipe supports one electrode. In Figure (19) these pipes are depicted as the long horizontal rectangles and the electrodes as the smaller vertical blocks. Each pipe can be manually slid in and out of the chamber to adjust the electrode seperation distance. Each electrode, as seen in Figure (20), rests inside a housing which connects to the pipe by a flat O-ring gasket with five Ultem hex head bolts.. The housing is a cylindrical metal cross-section with a base. Inside the base sits a smaller carbonate piece of the same design that isolates and insulates the current transmitted across the electrode from the housing. Inside the carbonate rest two equally sized steel discs, one of which is depicted in Figure (21). The metal surface that faces the plasma is six inches in diameter and has a smooth finish. On its inside there are five 1/11" wide holes with groves for the hex head bolts to catch drilled half way through as a way to join it via bolts to the rest of the housing. The other disc, which is unseen within, has the holes drilled all the way through. Each of the four pieces have these holes drilled through in the same place relative to their center so that they may be properly aligned with the Ultem bolts.

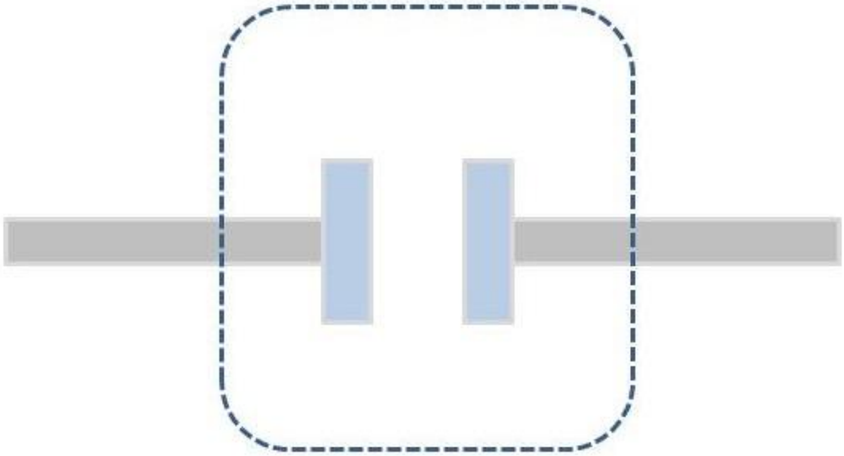

Figure 19 depicts the sealed pipes that connect the transmission lines to the back of the electrodes inside the process chamber.

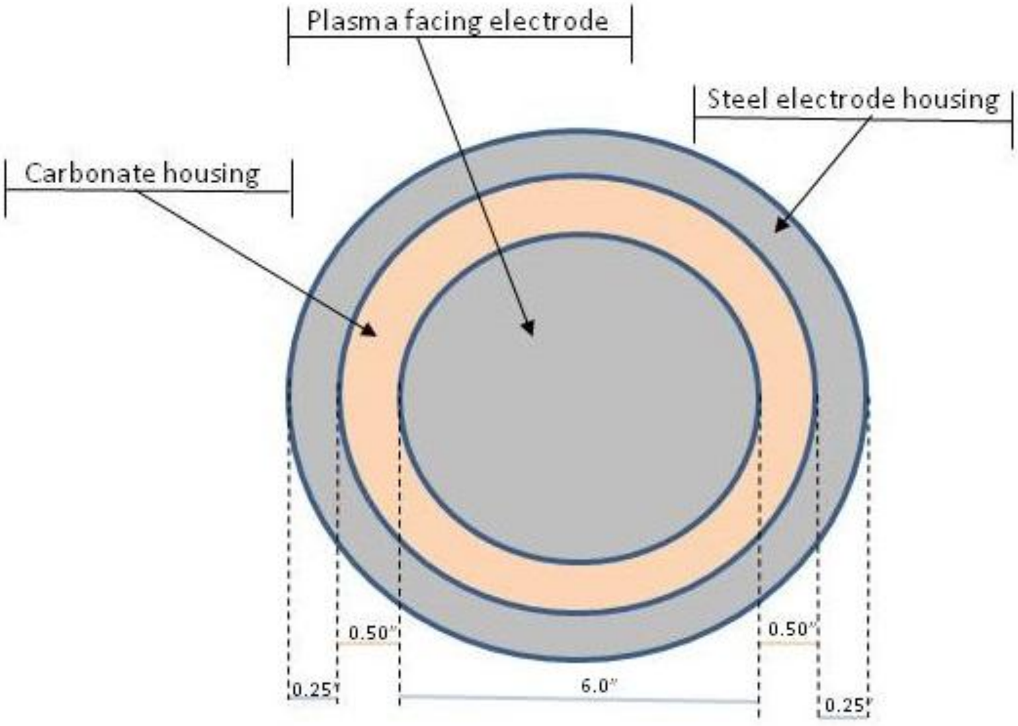

Figure 20 specifies the widths of each material housing that comprise the electrode.

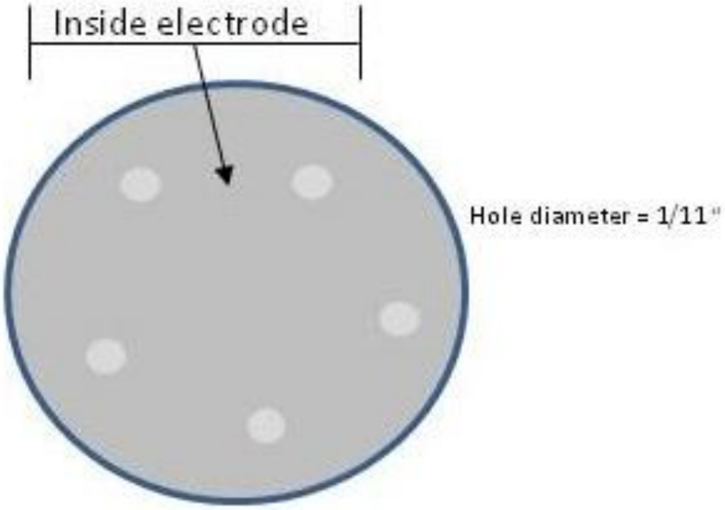

Figure 21 indicates the design pattern and diameter of the holes drilled in each plate to allow screws to hold the full electrode housing together.

There is a vast variation in chamber designs and system layouts. Figures (23) through (34) provide a visual tour of the size and relative layout of the process chamber and its collective operating equipment. Figure (22) is a much more detailed illustration of the various parts of the system and how they connect to one another.

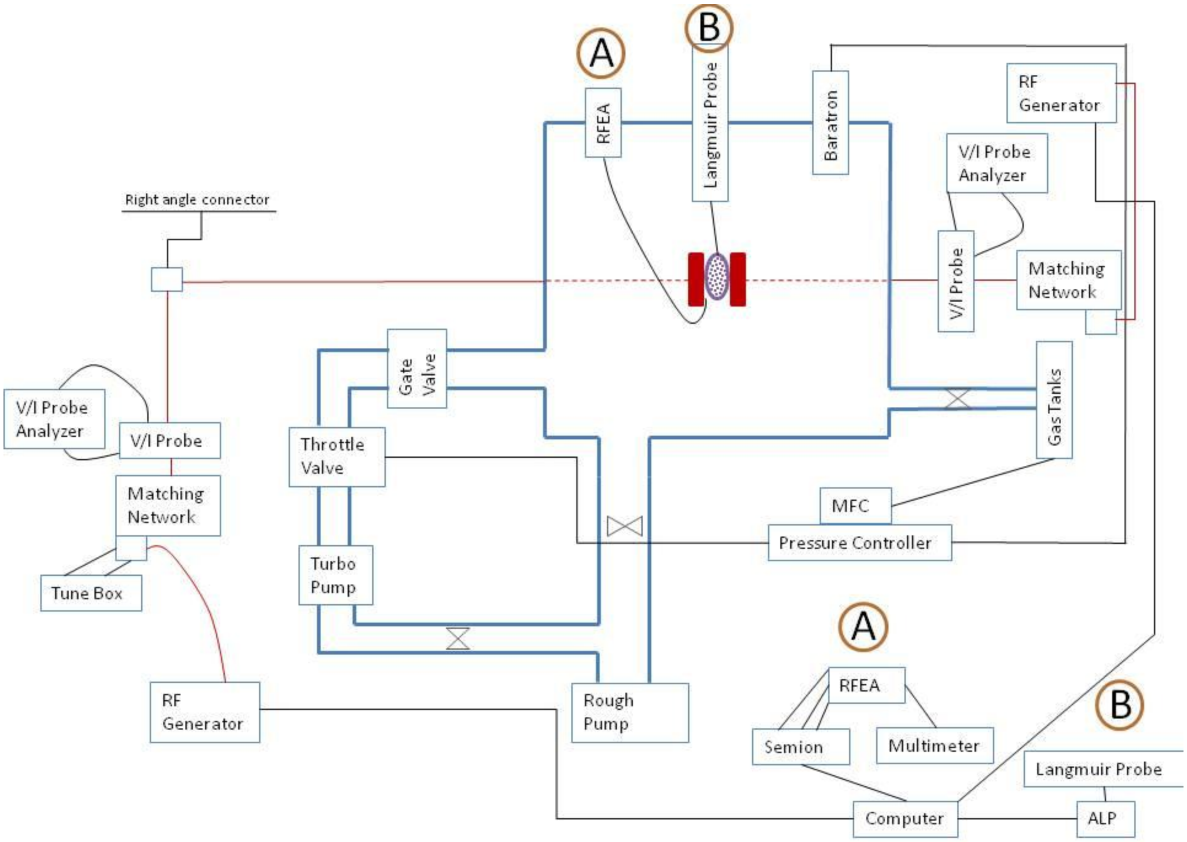

Figure 22: Sketch of the equipment placement and their respective connections for the entire system when driving dual frequency CCP.

Figure 23: CCP chamber and system view from front right.

Figure 24: CCP chamber and system view from front left.

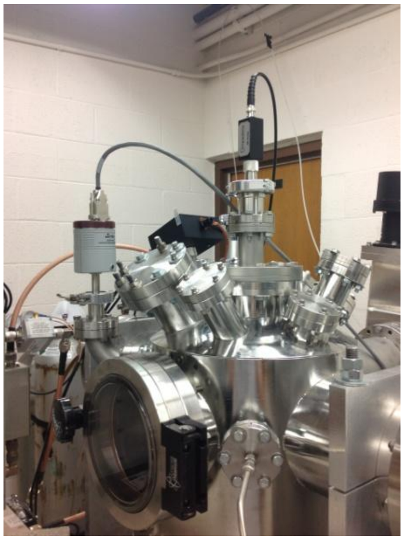

Figure 25: CCP chamber and system view from up close on right side, depicting the gas inlet in the bottom middle, the Langmuir Probe array at the top-center, the MKS Baratron sensor on the left, and the black RFEA filter box in between the Baratron and Langmuir Probe.

Figure 26: Gas tanks and their respected valves to admit gas flow into vacuum chamber.

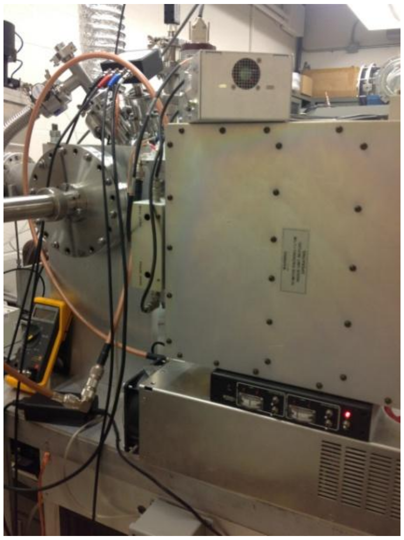

Figure 27: 13.56 MHz Matching Network with MKS bird probe analyzer on top, black tuning box is sandwiched between Match and Generator.

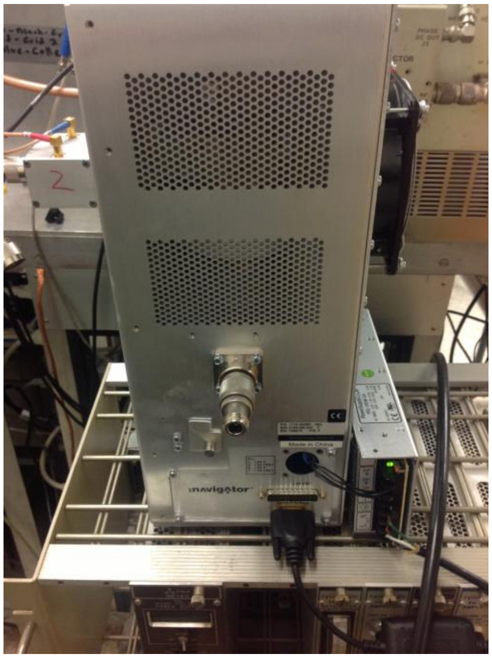

Figure 28 is a photograph of the 60 MHz generator used.

Figure 29: Alternate view of the Matching Network to show Bird Probe throughput and its connection to the analyzer.

Figure 30: Pressure valve that connects vacuum chamber to rough pump only.

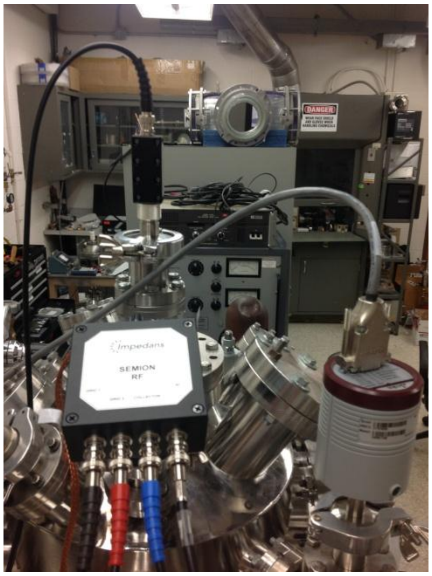

Figure 31: Front view on top of the chamber. Black Langmuir Probe sensor rising out of the top, black RFEA filter box with multi-colored cords, and Baratron Pressure gauge on the right.

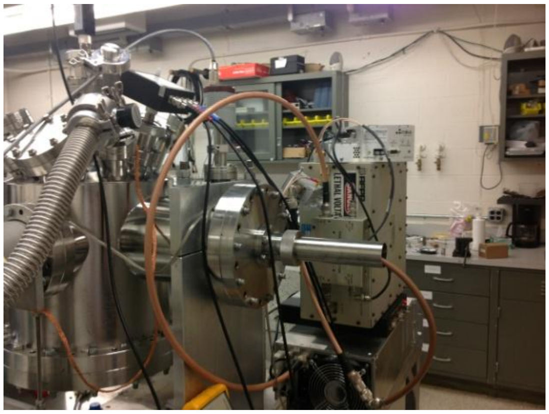

Figure 32: View of the system to illustrate the connection of the Matching Network to the Transmission Lines.

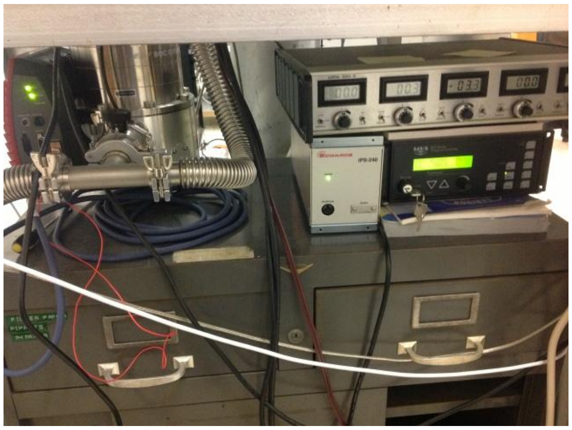

Figure 33: From left to right: Turbo pump and its respective pressure valve, Mass Flow controller sitting on top of Pressure Controller.

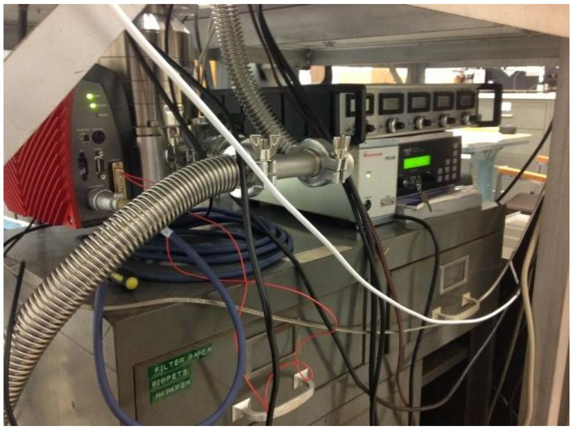

Figure 34: Same equipment seen in Figure 17 from a different angle to illustrate the vacuum tubing from the rough pump make a connection with the turbo pump and then on up to the chamber as seen in Figure 14.

Data collection for this process chamber can be taken in a several different configurations. If only one frequency is being applied to the plasma, the system will be laid out as shown in Figure (35), noting that either electrode may be hooked up as the powered electrode. In the case of the left electrode being powered, the red line from the RF generator to the matching network is Transmission Line 3, Transmission Line 2 connects the Match and V/I probe to a right angle connector, and Transmission Line 1 connects from there to the back of the left electrode. The right electrode is connected to Transmission Line 4, which in this scenario would be connected to ground. If the right electrode is chosen to be powered, Transmission Lines 1 and 2 are not used, and instead Transmission Line 4 connects to the matching network.

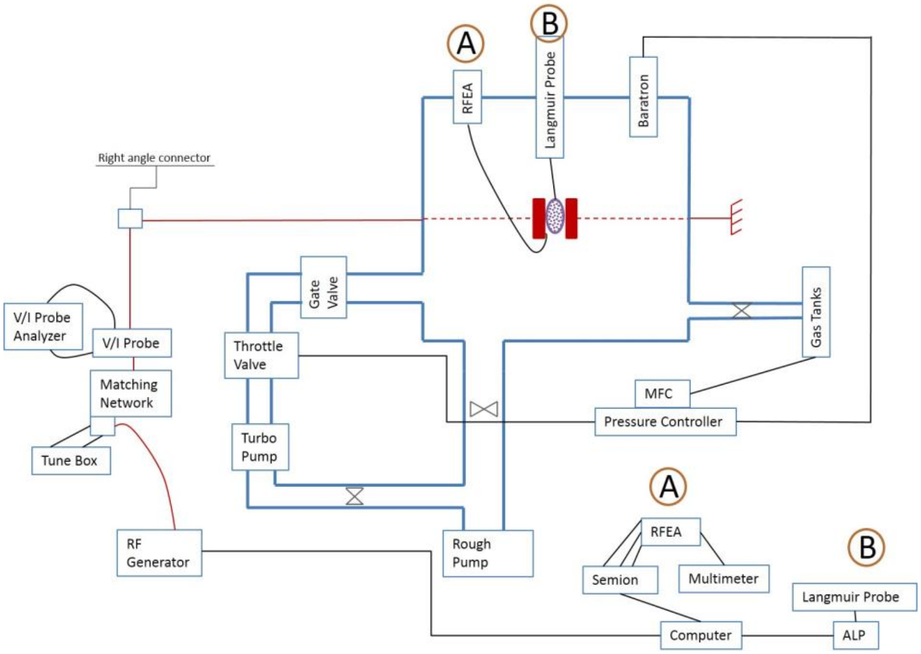

Figure 35: Sketch of the equipment placement and their respected connections for the entire system when operating one frequency.

If a dual frequency CCP is desired, Figure (22) depicts a similar set-up, with Transmission Line 4 connecting the right electrode to its respective matching network and a fifth Transmission Line would be needed to connect the match to an RF generator.

PART 4: Measurements, Results, and Discussion

Up to this point, the theory and model sections have outlined the background for running experimental data collection using a dual frequency capacitively coupled argon discharge. At the time of the writing of this thesis, the necessary equipment to drive two frequency generators simultaneously only became available several days prior to the official submission deadline of this work. As a result, the measurements concerning phase-locked dual frequency data and its subsequent analysis are sparse. However, using a single frequency generator driving either a 13.56 MHz or 60 MHz rf power supply, satisfactory IEDs have been attained for a range of pressures and power inputs that are in agreement with similar experimental results published by the community. Part 4 details which parameters are used as inputs in the measurement section, and then displays the results of this data. The last section in Part 4 elaborates on the trends and oddities seen in the resulting plots, as well as details possible improvements and faults that the system needs to have addressed.

Measurements

Two rf generators, a 13.56 MHz and a 60 MHz, and their respective matching networks were used to drive the powered electrode. Referencing Figure (35), the powered electrode was the left electrode, the grounded electrode (which has the RFEA sensor disc attached to its surface) is therefore the right electrode, and the Langmuir probe rests half way between both. The 13.56 MHz generator was driven at power inputs of 15, 25, 30, 40, 50, 60, 75, and 100 Watts, each at a pressure of 50, 100, and 200 mTorr. For reasons detailed in the Discussion section, the system could not consistently strike plasma at pressures lower than 50 mTorr. The 60 MHz generator cannot drive voltage at less than a 50 Watt input. Data was collected for the 60 MHz generator at power inputs of 50, 60, 75, and 100 Watts, using pressures of 10, 25, and 50 mTorr. The gas supplied to the chamber is always 0.102 ccm argon gas.

The RFEA probe floats at the dc bias V_{dc}. The required dc electric fields between the grids of the probe are produced by setting the grid potentials relative to V_{dc} rather than relative to ground. The probe filter box has a cable connecting it to a multi-meter to enable direct measurement of V_{dc}.

After the inputs are set and a discharge struck, the Langmuir probe software is used to determine the plasma potential, V_p. Next, the multi-meter supplies the required manual input for V_{dc} into the RFEA software. Once plots of the IEDs are generated, the corrected potential is determined by the summation of V_{dc} and V_p, illustrating the approximate midpoint of the bi-modal energy distributions. If more than one peak exists, then the corrected potential indicates the midpoint between the two peaks. The peak separation is approximately equivalent to the peak-to-peak sheath voltage. The data indicates that this IED profile occurs more often at high frequencies given that most of the 60 MHz rf IEDs have dual peaks in their plots.

Measurements and calculations designed to infer behavior trends about sheath thickness are gathered by first determining the half-minimum and half-maximum values of each IED voltage plot. The half-minimum value is subtracted from the half-maximum value to deduce the voltage width range for each distribution. Each power input and its voltage width results are plotted against one another within the same frequency regime. The trends for 13.56 MHz are significantly different than the trends for 60 MHz.

Data collected for phase-locked dual frequency IEDs utilized the same 13.56 MHz rf generator. The 60 MHz generator used previously was refitted to run at 27 MHz. Phase-locking between the two generators proved to be more difficult than originally thought. No tuning equipment currently exists on the market that can provide a precision measurement at the nano-frequency scale, thus acquiring a perfect phase-tuning between the two generators was impossible to match.

Results

The shape of the IED in collisionless rf plasma sheaths is predominantly determined by the ratio of the ion transit time to the period of the rf cycle.[18]

Discharges produced using intermediate rf regimes at low pressures produce single peak IEDs with increasing ion energy as power input is increased.

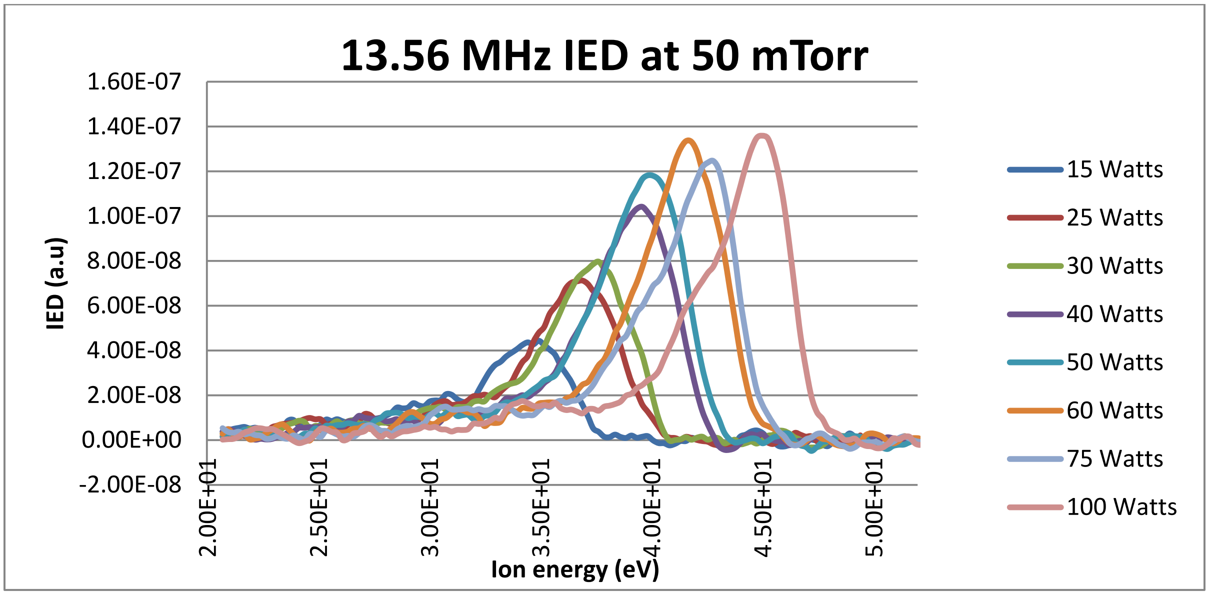

Figure 36: IEDs at 50mTorr for 13.56 MHz.

As pressure increases the ion energy peaks become wider. Table (2) provides a reference to the calculated values of the minimum and maximum ion energies as predicted by the model for the first six power selections. The predicted values are nearly identical to the minimum values of the ion energies but also predict greater maximum ion energy by between 2 and 5 eV.

Table 2: Maximum and minimum energies calculated by the model for six power selections at 13.56 MHz.

Power [Watts]	V_{low} [eV]	V_{high} [eV]
15	32.088	43.611
25	35.605	48.392
30	36.034	48.975
40	37.664	51.19
50	37.836	51.423
60	39.552	53.755

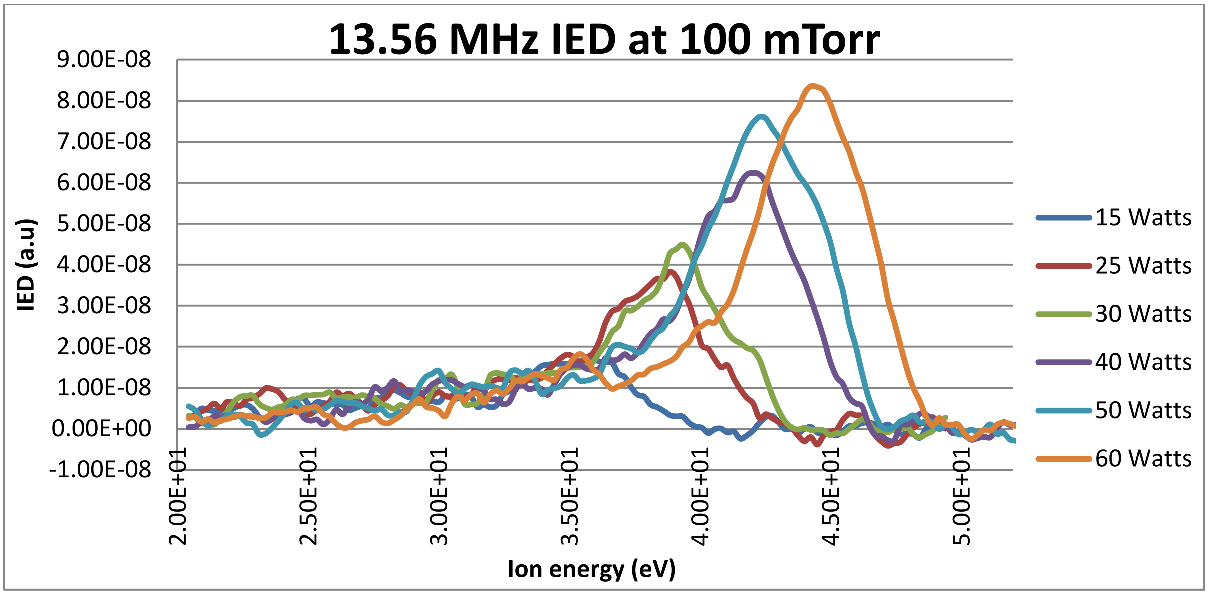

Figure 37: IEDs at 100mTorr for 13.56 MHz.

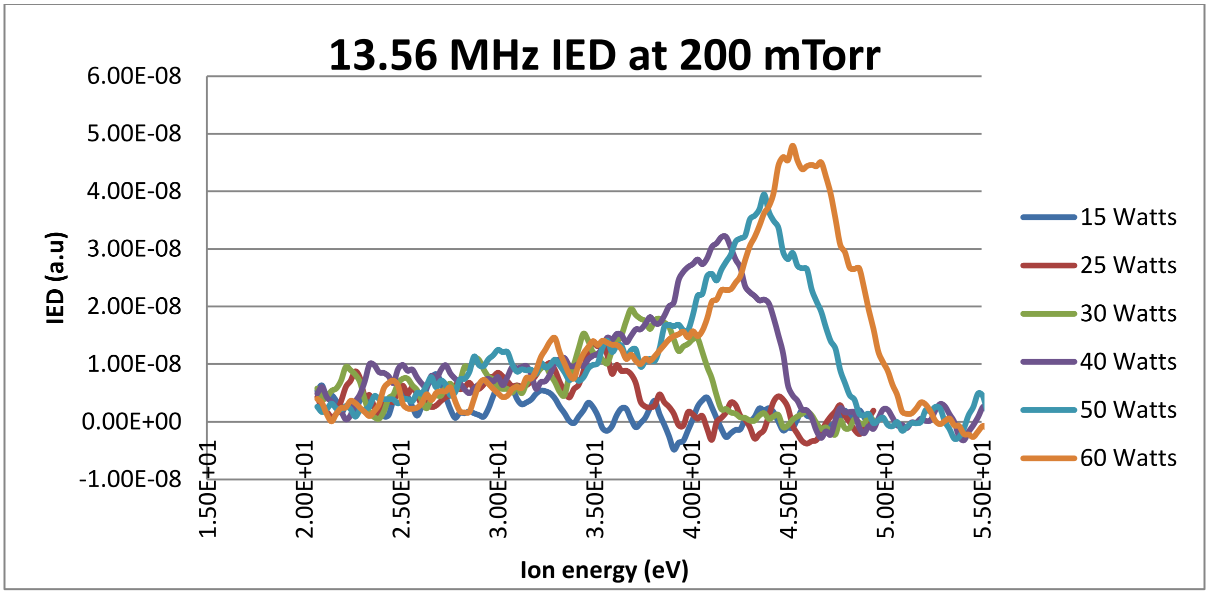

Figure 38: IEDs at 200mTorr for 13.56 MHz.

The series of peaks below the dominant peaks indicate that the ions undergo charge-exchange collisions within the sheath. As pressure increases, the sheath width also increases, and in turn increases the number of ion collisions undergone prior to being read by the RFEA.

There is likely some sort of error occurring for power input of 50 Watts at 10 mTorr, as seen in Figure (39), as it illustrates the only instance of all data collection runs with the lowest power input not resulting in the lowest ion energies. In the absence of this discrepancy, the height and separation of the two peaks increases with increasing power.

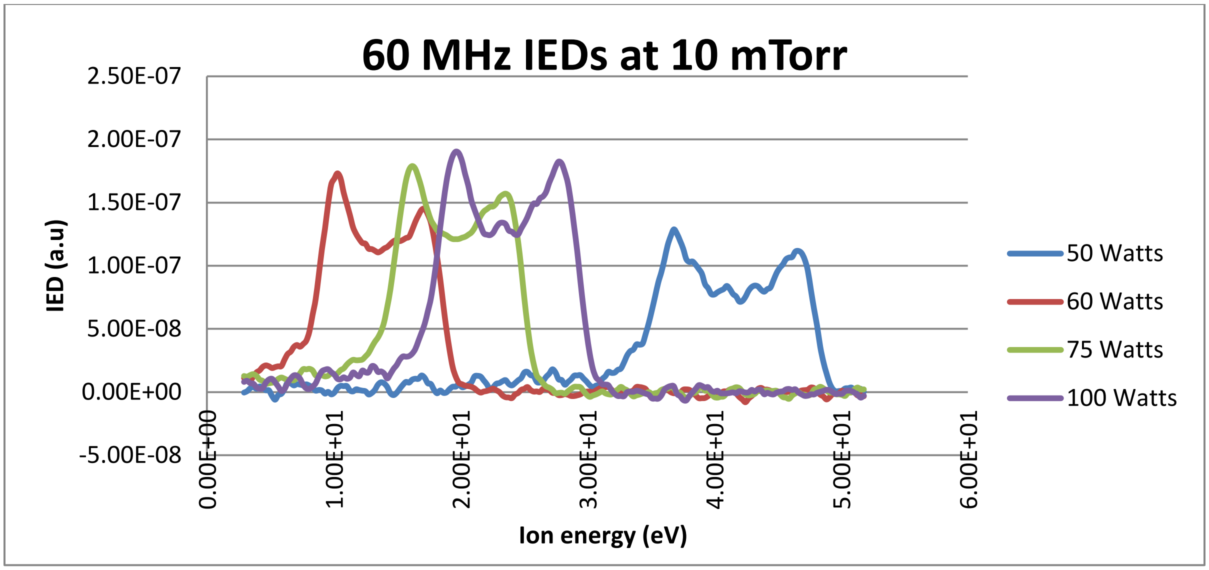

Figure 39: IEDs at 10mTorr for 60 MHz.

Contrary to what is seen at 13.56MHz, at 60 MHz, as pressure increases, IED width decreases.

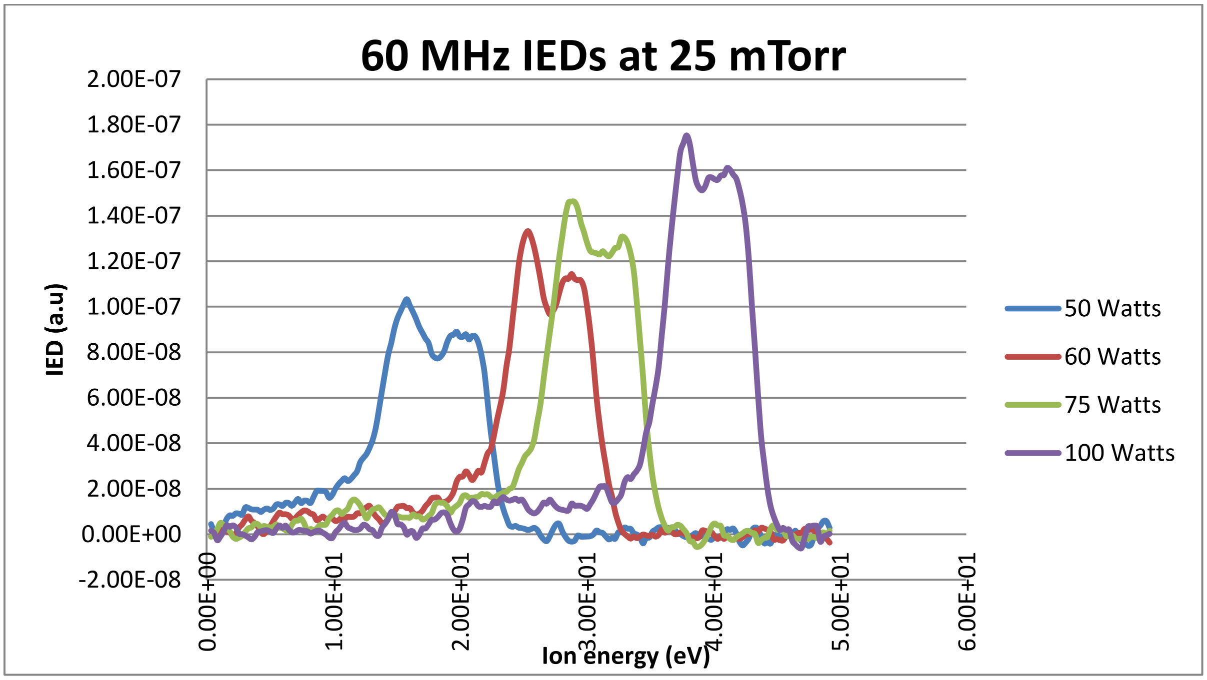

Figure 40: IEDs at 25mTorr for 60 MHz.

The saddle-shape created by two peaks seen in Figure (39) and (40) begins to smooth out toward one peak as pressure increases.

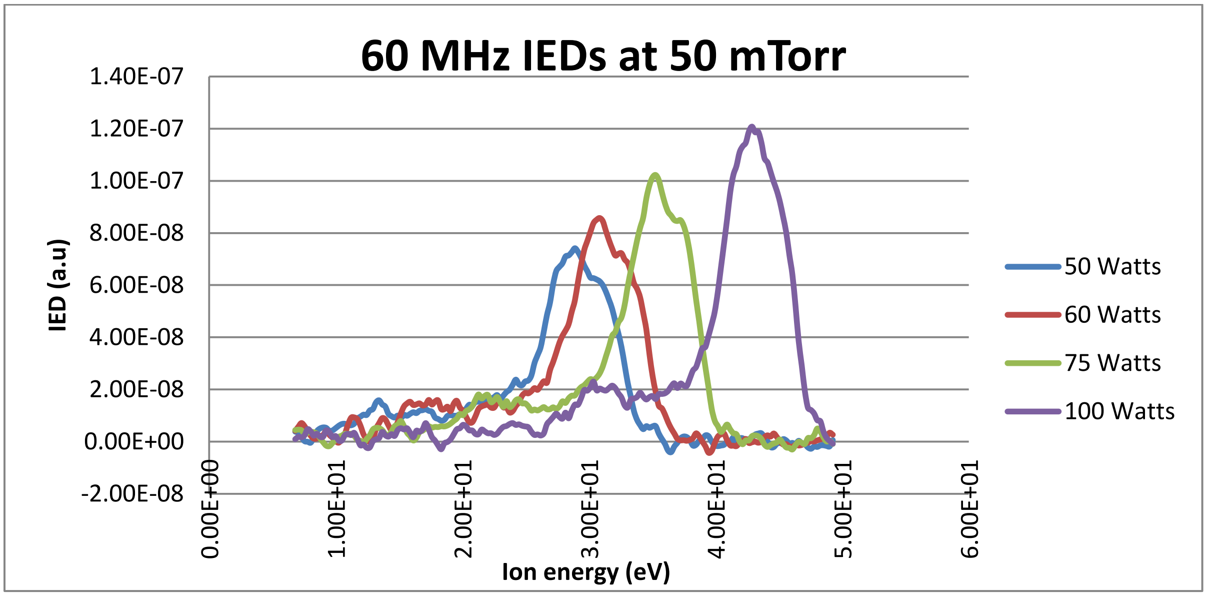

Figure 41: IEDs at 50mTorr for 60 MHz.

When compared to the Model using only one frequency the minimum and maximum ion energies the experimental results are a within ± 2 eV of those depicted in Figure (43). The theoretical results for a 60 MHz argon discharge at 50 mTorr for power inputs of 50, 60, 75, and 100 Watts are displayed in Table (3).

Table 3: Maximum and minimum energies calculated by the model for four power selections at 60 MHz.

Power [Watts]	V_{low} [eV]	V_{high} [eV]
50	28.674	35.901
60	30.544	38.242
75	34.284	42.925
100	41.402	51.844

Comparison between 13.56 and 60 MHz

At 50 mTorr, both 13.56 MHz and 60 MHz form single peak IEDs at 100 Watt inputs with nearly identical energy magnitudes. However, at lower power the 13.56 MHz produces greater ion energies. This is likely due to resonant charge transfer occurring between fast moving charged ions and slow moving neutral atoms passing each other within the sheath. This results in fewer ions reaching the detector as well as decreasing the effective energy of some ions that are detected. The noisy data seen at the low energies in Figure (43) are an indication of such an issue, and this noise is absent in the lower frequency data for the same set points shown in Figure (42).

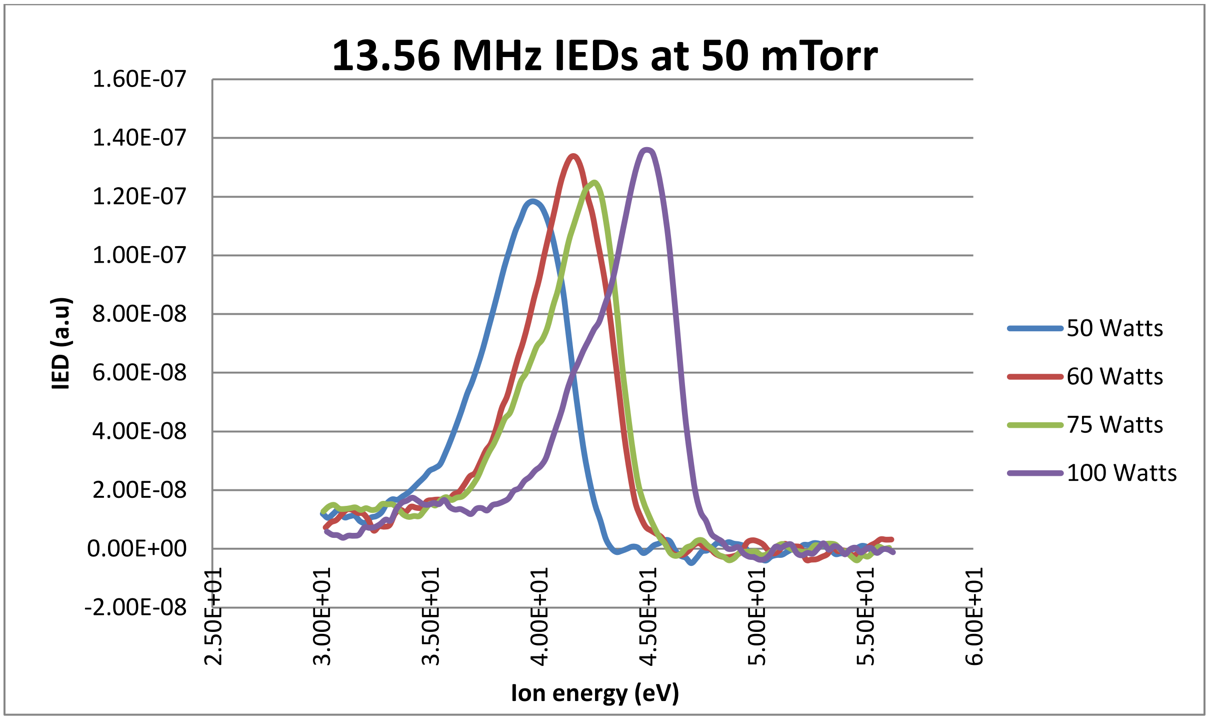

Figure 42: IEDs at 50mTorr for 13.56 MHz.

At increased frequency, the saddle-shape of dual peaks is just beginning to show, while the 13.56 MHz distributions maintain a dominant single peak with minimum secondary collisions.

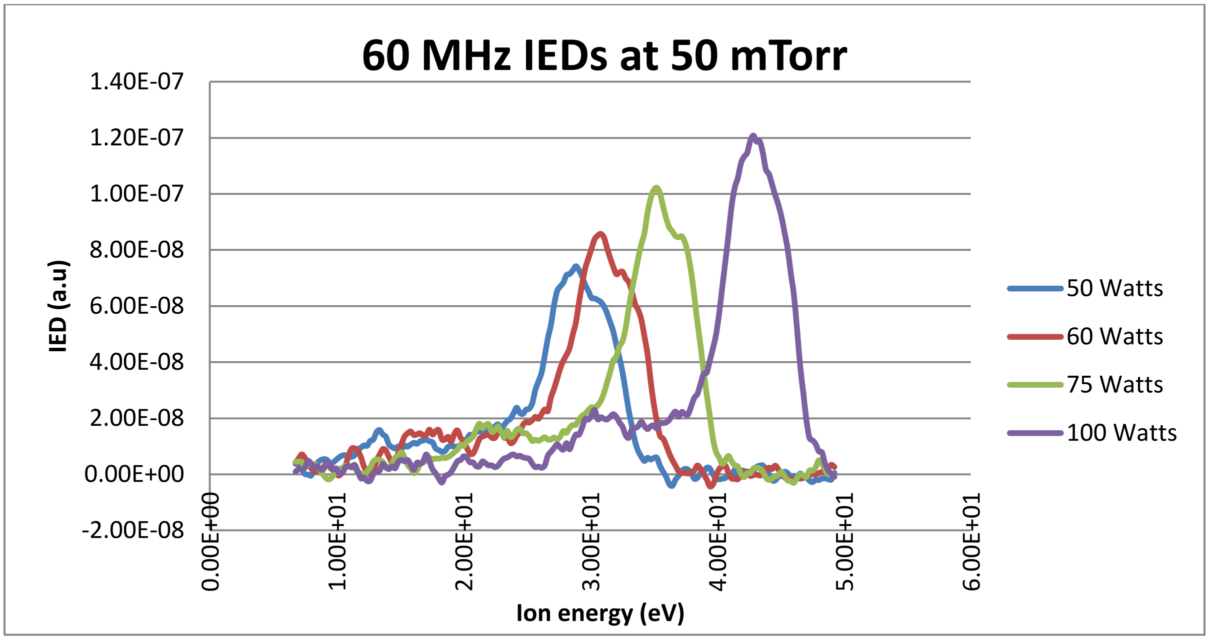

Figure 43: IEDs at 50mTorr for 60 MHz.

Voltage width distribution follows different trends from 13.56 MHz to 60 MHz. In regards to the former, voltage width distributions decrease as pressure decreases, but for the latter the distributions increase, as seen in Figure (44) and (45), respectively.

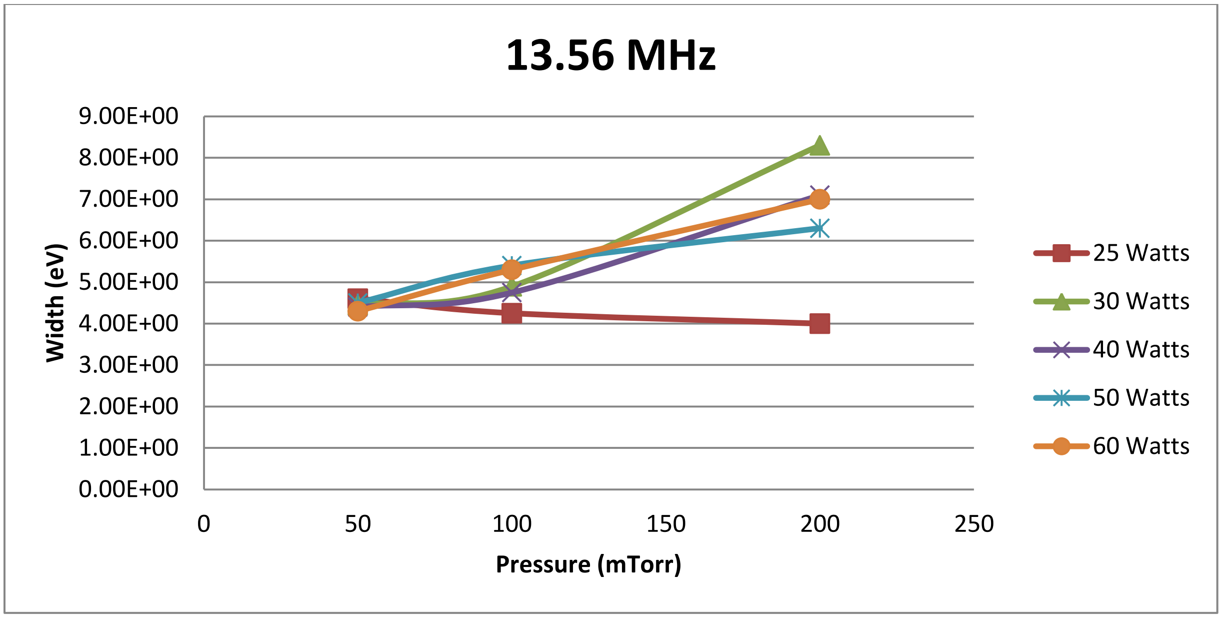

Figure 44 depicts the half-min and half-max width difference for various power inputs for 13.56 MHz measurements as pressure decrease.

Voltage width ranges for IEDs using 13.56 MHz are negligibly affected by decreases in pressure.

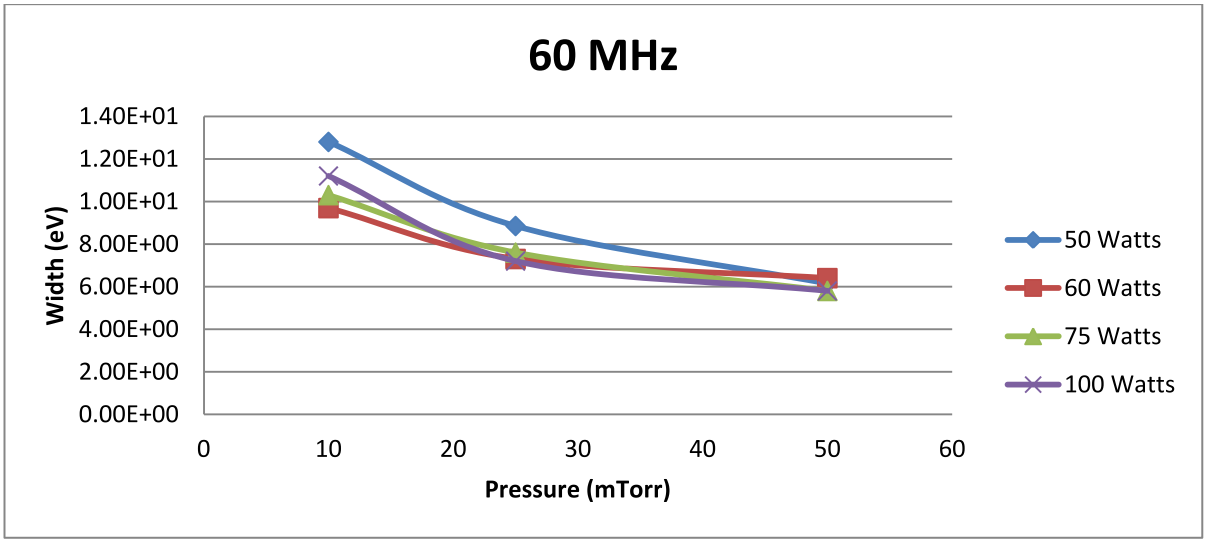

Figure 45 depicts the half-min and half-max width difference for various power inputs for 60 MHz measurements as pressure decreases.

The voltage width range will depend on sheath thickness, which in turn depends of pressure. At 60 MHz the width is increasing with decreasing pressure because the sheath is expanding. As the sheath expands there will be more collisions amongst ions, resulting in a wider range of IED voltages.

The plot shown in Figure (46) is an excerpt from of a dual frequency sweep of 13.56 MHz and 27 MHz at 25mTorr running 50 Watts in both generators.

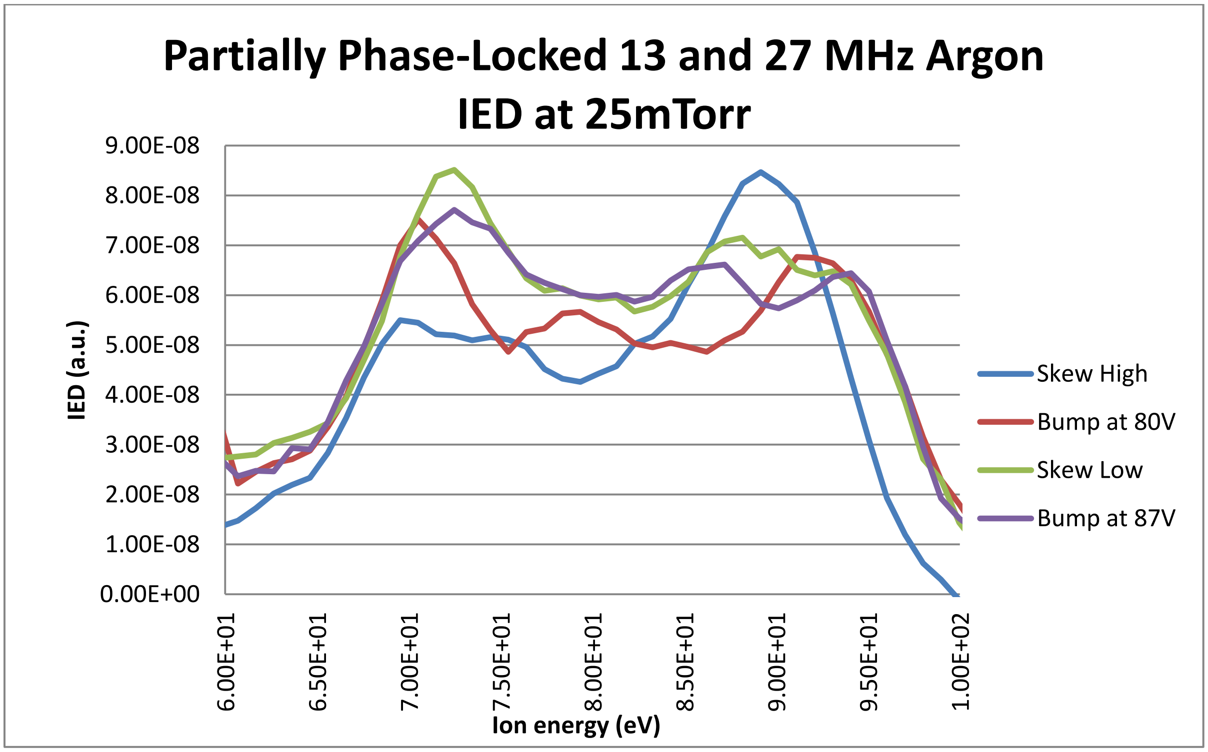

Figure 46 depicts a successful coupling of two frequencies using M.K.S. equipment.

Discussion

The experimental data is consistent with the model for single frequency, albeit the model predicts slightly higher ion energy maximums. However, when plotting the IEDs in the figures above prior to checking them against the model, it was identified that the experimental peaks were slightly less than the expected midpoints determined by the corrected plasma potentials. This may be due to a leak in the vacuum chamber. The filter box attached to the RFEA probe also serves as a conduit between the inside and outside of the process chamber. It is now known to have a faulty vacuum seal. This leak has allowed air (and all the gases it's composed of) to seep into the chamber and contaminate the pure argon gas composition.

Despite having a symmetric geometry, the plasma will always produce an asymmetric sheath profile because the sheath on the powered electrode is significantly larger than the sheath on the grounded electrode. This result is more collisions in the powered sheath and thus the frequency model, as written, will fall apart (since it is designed for collisionless sheaths). This, however, can be resolved by placing the RFEA probe on the grounded electrode.

PART 5: Conclusion and Future Work

Using a mathematical model to generate approximate ion energy distributions for single or dual frequency capacitively coupled rf plasmas was successfully validated using a retarding field energy analyzer in conjunction with a Langmuir probe. The model also hypothesizes IEDs for phase-locked dual frequency CCP, but ample data could not be collected experimentally to verify the model due to lack of proper equipment and hardware availability prior to the thesis submission deadline. However, since the model is derived from a proven model and has performed accurately with predicting similar IEDs that were collected experimentally, there is a valid indication that it will also work for future experiments utilizing dual frequency phase-locked rf generators at 13.56 MHz and 27 MHz. Also, the limited data collected using partially phase-locked dual frequency rf generators provides further validation of the model.

There is still much to be desired in the particular system used, such as a filter box for the RFEA that is properly vacuumed sealed, no issue running both Impedans software for the Langmuir probe and the RFEA simultaneously; and a 27 MHz generator to verify the validity of the phase effect for this model. These are all future prospects for this system, and fortunately, they each are realistic goals for the near future, but were not available at the time of writing this thesis. Upgrading to the highest model of Impedans RFEAs would enable greater precision as well as allow for time-resolved measurements. The current model does not possess the proper sensors to provide built-in time resolved measurements. This limitation can be moderately combated by decreasing the scan time as much as possible by limiting the scan range and the scan resolution, then running twenty or more scans in quick succession. Watching the plot output on the computer monitor as the results display one scan after another simulates a time-resolved measurement with a time-step equal to that of any individual scan time length.

Another prospective improvement is to run more process comparisons between 13.56 MHz and 60 MHz within pressure and power regimes that overlap between the capabilities of both generators and their respective software. Other future endeavors could be to test this theory on inductively coupled plasma, as well as catalog results for a wider range of gases and gas compositions.

Works Cited

[1] Bogaerts A, Neyts E, Gijbels R, van der Mullen J. 2001. Gas discharge plasmas and their applications. Spectrochimica Acta Part B **57**: 609-658.

[2] https://commons.wikimedia.org/wiki/File:Gase-in-Entladungsroehren.jpg

[3] Lieberman MA, Lichtenberg AJ. 2005. Principles of plasma discharges and materials processing. 2nd ed. Hoboken, NJ: John Wiley & Sons, Inc. 388 p.

[4] Fridman A, Kennedy LA. 2011. Plasma physics and engineering. 2nd ed. Boca Raton, FL: CRC Press. 646 p.

[5] Lieberman MA, Lichtenberg AJ. 2005. Principles of plasma discharges and materials processing. 2nd ed. Hoboken, NJ: John Wiley & Sons, Inc. 471-472.

[6] d'Agostino R, Favia P, Kawai Y, Ikegami H, Sato N, Arefi-Khonsari F, editors. 2008. Advanced Plasma Technology. Germany: Wiley-VHC. 22 p.

[7] Beckerle JC. 1953. Exchange between rotational and translational energy in gas molecules. J. Chem. Phys. **21**(11): 2034-2041.

[8] Lee JK, Babaeva NY, Kim HC, Manuilenko OV, Shon JW. 2004. Simulation of capacitively coupled single- and dual-frequency rf discharges. IEEE Transactions on Plasma Science **32**(1): 47-53.

[9] Kawamura E, Vahedi V, Lieberman MA, Birdsall CK. 1999. Ion energy distributions in rf sheaths; review, analysis and simulation. Plasma Sources Sci. Technol. **8**(1): R45-R64.

[10] van Roosmalen AJ, Baggerman JAG, Brader SJH. 1991. Dry etching for VLSI. New York, NY: Plenum Press. 30 p.

[11] Verdonck P. 1996. Plasma Etching. V Oficina de Microelectronica [internet]. Available from: http://www.ccs.unicamp.br/cursos/fee107/download/cap10.pdf

[12] Heil BG, Czarnetzki U, Brinkmann RP, Mussenbrock T. 2008. On the possibility of making a geometrically symmetric RF-CCP discharge electrically asymmetric. J. Phys. D: Appl. Phys. **41** 165202: 1-19.

[13] Buzzi FL, Ting YH, Wendt AE. 2009. Energy distribution of bombarding ions in plasma etching of dielectrics. Plasma Sources Sci. Technol. **18** 025009: 1-8.

[14] Fridman A, Kennedy LA. 2011. Plasma physics and engineering. 2nd ed. Boca Raton, FL: CRC Press. 678-679 p.

[15] Wang SB, Wendt AE. 2001. Ion bombardment energy and SiO_2/Si fluorocarbon plasma etch selectivity. J. Vac. Sci. Technol. A **19**(5): 2425-2432.

[16] Shannon S, Hoffman D, Yang JG, Paterson A, Holland J. 2005. The impact of frequency mixing on sheath properties: Ion energy distribution and V_{dc}/V_{rf} interaction. J. Appl. Phys. **97** 103304: 1-4.

[17] Liu J, Wang J, Shannon S, Kim JM, Shin T, Shoji S, Detrick T, Pu B. c2005. Dual frequency bias power benefits on dielectric etch chamber. Proceedings of the 26th International Symposium on Dry Process. P.359-364.

[18] Panagopoulos T, Economou DJ. 1999. Plasma sheath model and ion energy distribution for all radio frequencies. J. Appl. Phys. **85**(7): 3435-3443.

[19] Impedans. Semion RFEA System Installation & User Guide. Revision: 2.7. Approved 12-08-12. 60 p.

[20] Gahan D, Daniels S, Hayden C, O'Sullivan C, Hopkins MB. 2011. Characterization of an asymmetric parallel plate radio-frequency discharge using a retarding field energy analyzer. Plasma Sources Sci. Technol. **21** 015002: 1-12.

Appendix

Appendix A

IEDF Calculation Overview

Example Discharge using Argon gas.

RF Drive Set points: fraction of low frequency power over high frequency power is x. So an x value of 1 is when there is no power contribution from the higher frequency generator. Set up a base frequency f, a high frequency harmonic defined by $n \cdot f$, and a phase component φ.

Peak currents are determined by single frequency current to generate a given DC potential:

$$I_{low} = x\sqrt{-8\pi^2 V_{dc}\varepsilon_0 e n_e f^2 Area^2} \tag{1}$$

$$I_{high} = (1-x)\sqrt{-8\pi^2 V_{dc}\varepsilon_0 e n_e (nf)^2\ Area^2} \tag{2}$$

These can be rewritten as:

$$I_{low} = x\frac{Area(2\pi f)}{3}\sqrt{-6\cdot 2V_{dc}\varepsilon_0 e n_e} \tag{3}$$

$$I_{high} = (1-x)\frac{Area(2\pi nf)}{3}\sqrt{-6\cdot 2V_{dc}\varepsilon_0 e n_e} \tag{4}$$

The next step is to determine the sheath widths based on the high and low current, remembering that the "high" relationship always refers to the multiplication of the drive frequency by the chosen harmonic value, *n*. The time-averaged sheath thickness, S_0, is the sum of the low and high components of the sheath amplitude, and $S(t)$ is the time-varying oscillation of a single sheath driven by both high and low frequencies.

$$s_{low} = \frac{I_{low}}{e n_e 2\pi f\,(Area)} \tag{5}$$

$$s_{high} = \frac{I_{high}}{e n_e 2\pi nf\,(Area)} \tag{6}$$

$$s_0 = s_{low} + s_{high} \tag{7}$$

$$s(t)=s_{low}+s_{high}+s_{low}\sin(2\pi ft)+s_{high}\sin(2\pi nft+\varphi) \tag{8}$$

The transit time for an ion across the sheath is defined by τ_i.

$$\tau_i=3s_0\sqrt{\frac{m_i}{2eV_{dc}}} \tag{9}$$

By substituting equation (8) into equation (10) the sheath potential for the system can be calculated by treating it as a parallel plate vacuum capacitor holding a charge of $en_e/2$ with a time-varying gap equal to S_0, resulting in Equation (11). Purely as a means to shorten the lengths of the equations, Equations (12) is defined and subsequently the sheath potential is rewritten in Equation (13).

Sheath potential:

$$V_{sheath}(t)=-\frac{en_e}{2\varepsilon_0}s(t)^2 \tag{10}$$

$$V_{sheath}(t)=-\frac{en_e}{2\varepsilon_0}\left[s_{low}+s_{high}+s_{low}\sin(2\pi ft)+s_{high}\sin(2\pi nft+\varphi)\right]^2 \tag{11}$$

$$\omega=2\pi f \tag{12}$$

$$V_{sheath}(t)=-\frac{en_e}{2\varepsilon_0}\left[s_{low}+s_{high}+s_{low}\sin(\omega t)+s_{high}\sin(n\omega t+\varphi)\right]^2 \tag{13}$$

The ions see a damped potential in the sheath where the magnitude of the oscillation is damped by:

Knowing each frequency component of the sheath potential allows for the derivation of an ion apparent potential, where the amplitude of each frequency is damped or weighted by a $1/\omega\tau_i$ term. The sheath voltage needs to be broken up into frequency components to capture this for multiple frequencies. Equation (14) displays the squared out expression inside the brackets from Equation (13).

$$\begin{gathered}\left(s_{low}+s_{high}\right)^2+2\left(s_{low}+s_{high}\right)s_{low}\sin(\omega t)+2s_{high}\left(s_{low}+s_{high}\right)\sin(n\omega t+\varphi)+s_{low}^2\sin^2(\omega t)+\\ 2s_{low}s_{high}\sin(n\omega t+\varphi)\sin(\omega t)+s_{high}^2\sin^2(n\omega t+\varphi)\end{gathered} \tag{14}$$

Using double angle trigonometric identities from Equations (15) and (16), the fully expanded expression from Equation (13) can be solved. This is expressed in Equation (17).

$$\sin^2(\omega t)\equiv\frac{1}{2}-\frac{\cos(2\omega t)}{2} \qquad \sin^2(n\omega t+\varphi)\equiv\frac{1}{2}-\frac{\cos(2n\omega t+2\varphi)}{2} \tag{15}$$

$$\sin\left(n\omega t+\varphi\right)\sin\left(\omega t\right)\equiv\frac{1}{2}\left\{\cos\left[\omega t\left(n-1\right)+\varphi\right]-\cos\left[\omega t\left(n+1\right)+\varphi\right]\right\} \tag{16}$$

$$\begin{aligned}&\left(s_{low}+s_{high}\right)^2+2\left(s_{low}+s_{high}\right)s_{low}\sin\left(\omega t\right)+2s_{high}\left(s_{low}+s_{high}\right)\sin\left(n\omega t+\varphi\right)+s_{low}^2\left(\frac{1}{2}-\frac{\cos\left(2\omega t\right)}{2}\right)+\\&2s_{low}s_{high}\frac{1}{2}\left\{\cos\left[\omega t\left(n-1\right)+\varphi\right]-\cos\left[\omega t\left(n+1\right)+\varphi\right]\right\}+s_{high}^2\left(\frac{1}{2}-\frac{\cos\left(2n\omega t+2\varphi\right)}{2}\right)\end{aligned} \tag{17}$$

The multiple components of the frequency are broken down into four categories: DC, Fundamental, Harmonic, and Mixing.

DC Component:

$$\frac{3}{2}s_{low}^2+\frac{3}{2}s_{high}^2+2s_{low}s_{high} \tag{18}$$

Fundamental Component:

$$2s_{low}\left(s_{low}+s_{high}\right)\sin\left(\omega t\right)+2s_{high}\left(s_{low}+s_{high}\right)\sin\left(n\omega t+\varphi\right) \tag{19}$$

Harmonic Component:

$$-\frac{1}{2}s_{low}^2\cos\left(2\omega t\right)-\frac{1}{2}s_{high}^2\cos\left(2n\omega t+2\varphi\right) \tag{20}$$

Mixing Component:

$$s_{low}s_{high}\left\{\cos\left[\omega t\left(n-1\right)+\varphi\right]-\cos\left[\omega t\left(n+1\right)+\varphi\right]\right\} \tag{21}$$

By combining these four components the time-varying sheath voltage is established in Equation (22):

$$V_{sheath}\left(t\right)=-\frac{en_e}{2\varepsilon_0}\begin{bmatrix}\frac{3}{2}s_{low}^2+\frac{3}{2}s_{high}^2+2s_{low}s_{high}+2s_{low}\left(s_{low}+s_{high}\right)\sin\left(\omega t\right)+2s_{high}\left(s_{low}+s_{high}\right)\sin\left(n\omega t+\varphi\right)\\-\frac{1}{2}s_{low}^2\cos\left(2\omega t\right)-\frac{1}{2}s_{high}^2\cos\left(2n\omega t+2\varphi\right)+s_{low}s_{high}\left\{\cos\left[\omega t\left(n-1\right)+\varphi\right]-\cos\left[\omega t\left(n+1\right)+\varphi\right]\right\}\end{bmatrix} \tag{22}$$

The voltage that the ion sees is damped by the $1/\omega\tau_i$ term. Each frequency component with a phase influence needs to be damped to that component's frequency. The full time-varying ion potential is expressed in Equation (23).

$$V_{ion}(t) = -\frac{en_e}{2\varepsilon_0}\left[\begin{array}{l} \frac{3}{2}s_{low}^2 + \frac{3}{2}s_{high}^2 + 2s_{low}s_{high} + \frac{2s_{low}\left(s_{low}+s_{high}\right)}{\omega\tau_i}\sin(\omega t) + \frac{2s_{high}\left(s_{low}+s_{high}\right)}{\omega n\tau_i}\sin(n\omega t+\varphi) \\ -\frac{1}{2}\frac{s_{low}^2}{4\omega\tau_i}\cos(2\omega t) - \frac{1}{2}\frac{s_{high}^2}{4n\omega\tau_i}\cos(2n\omega t+2\varphi) + \frac{s_{low}s_{high}}{\omega(n-1)\tau_i}\cos\left[\omega t(n-1)+\varphi\right] - \frac{s_{low}s_{high}}{\omega(n+1)\tau_i}\cos\left[\omega t(n+1)+\varphi\right] \end{array}\right] \quad (23)$$

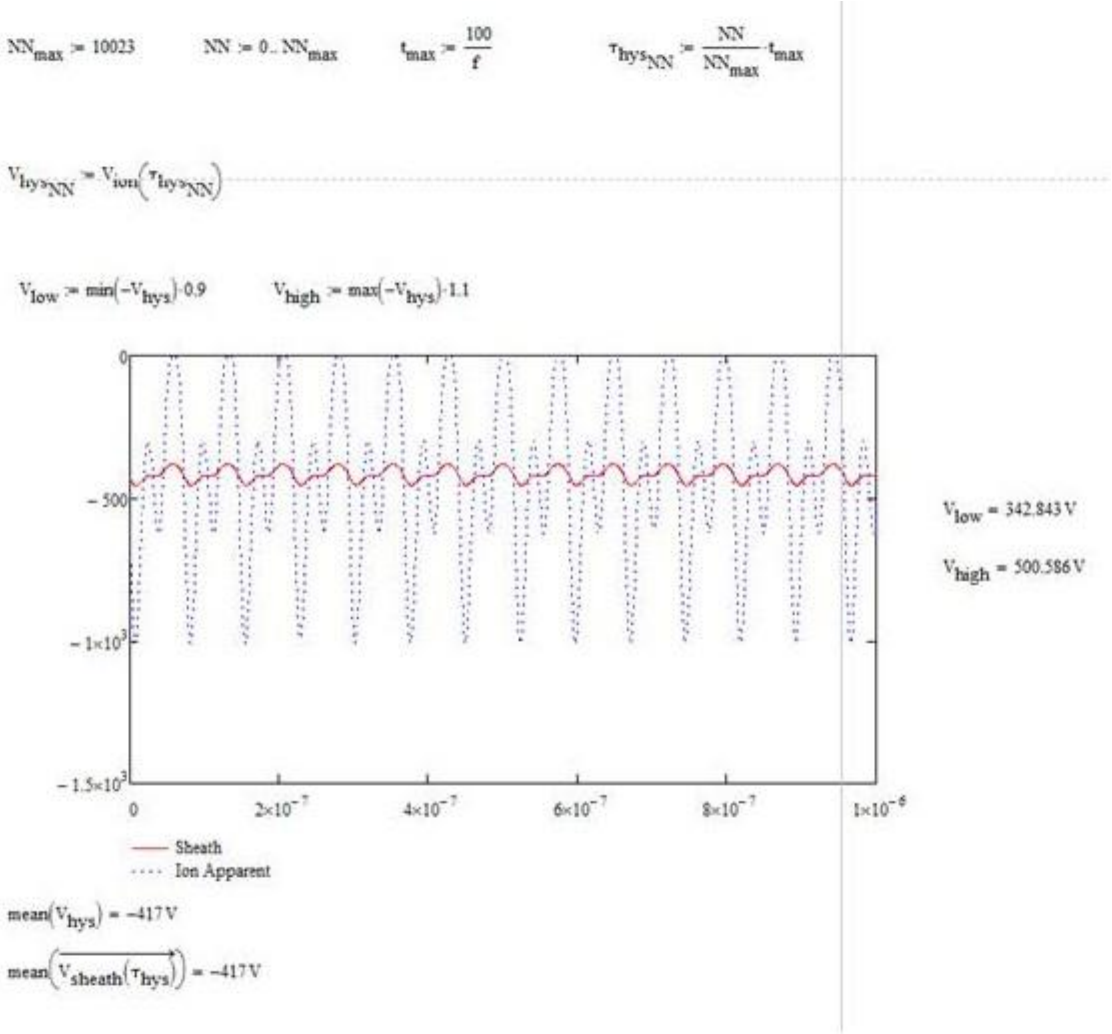

$NN_{max} := 10023$ $NN := 0..NN_{max}$ $t_{max} := \frac{100}{f}$ $\tau_{hys_{NN}} := \frac{NN}{NN_{max}} \cdot t_{max}$

$V_{hys_{NN}} := V_{ion}\left(\tau_{hys_{NN}}\right)$

$V_{low} := \min\left(-V_{hys}\right) \cdot 0.9$ $V_{high} := \max\left(-V_{hys}\right) \cdot 1.1$

$V_{low} = 342.843\,V$

$V_{high} = 500.586\,V$

$\text{mean}\left(V_{hys}\right) = -417\,V$

$\text{mean}\left(\overrightarrow{V_{sheath}\left(\tau_{hys}\right)}\right) = -417\,V$

Figure 47 depicts the oscillation of the sheath with respect to the ion apparent voltage for the set parameters with accompanying MathCad input code.

Now look at the histogram generated IEDF by binning the waveform with respect to time interval.

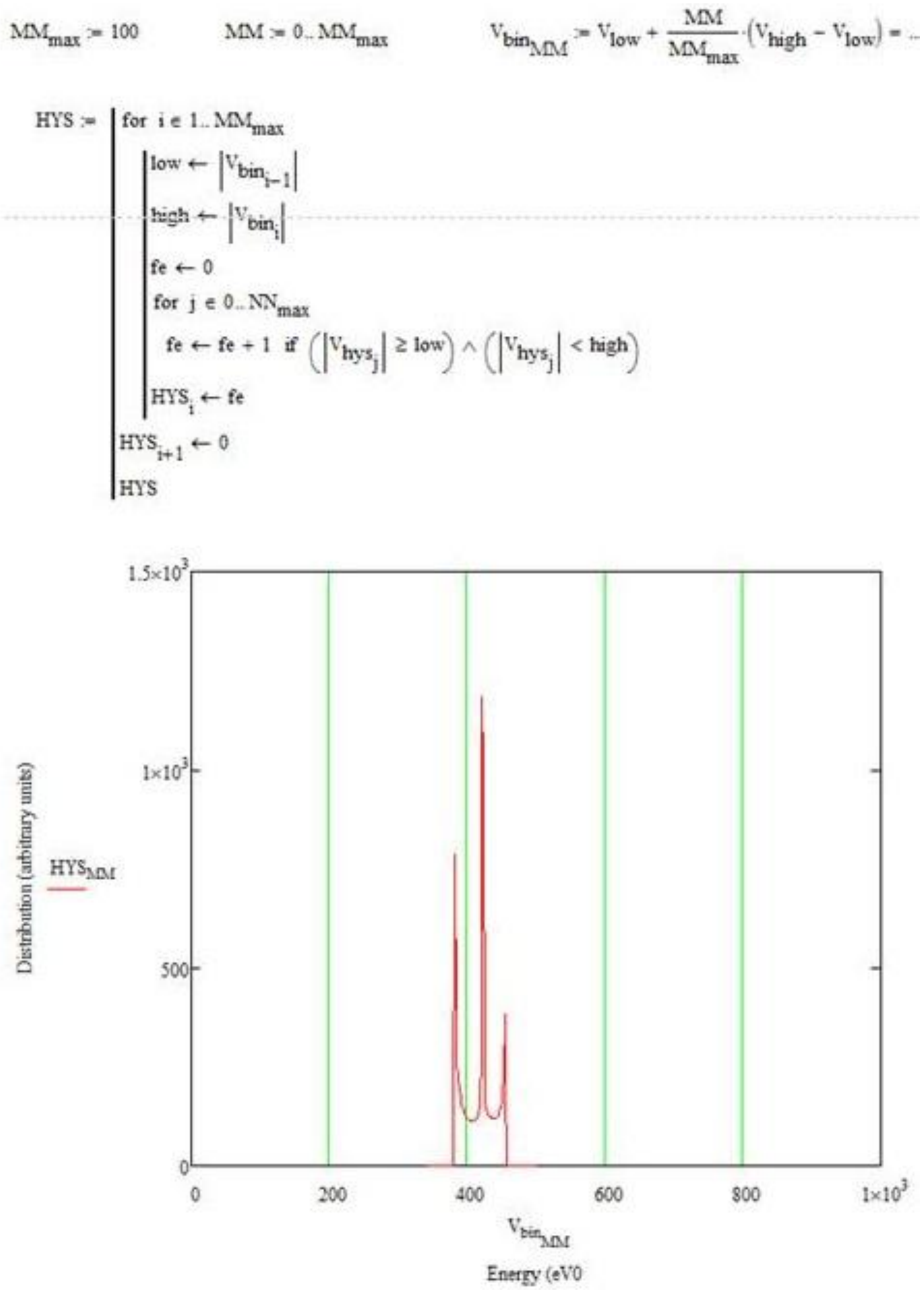

$MM_{max} := 100$ $\quad MM := 0..MM_{max}$ $\quad V_{bin_{MM}} := V_{low} + \frac{MM}{MM_{max}} \cdot (V_{high} - V_{low}) = ..$

```
HYS := | for  i ∈ 1..MM_max
       |    | low ← |V_bin_(i−1)|
       |    | high ← |V_bin_i|
       |    | fe ← 0
       |    | for  j ∈ 0..NN_max
       |    |    fe ← fe + 1  if  (|V_hys_j| ≥ low) ∧ (|V_hys_j| < high)
       |    | HYS_i ← fe
       | HYS_(i+1) ← 0
       | HYS
```

Figure 48 depicts the histogram for the set parameters as solved by MathCad with accompanying input code to create plot.

Appendix B

Matlab Code

The “.m” files tau, sheath_parameters, and peak_currents, do not call on any other functions. So they are required to be defined first.

{tau.m}

```
%%%%%%%%%%%%%%%%%%%%%%%%%%%%%%%%%%%%%%%%
% Calculates the tau_i critical parameter
% (ref: Kawamura, Vahedi, Lieberman, Birdsall)
%   s_0  := s_low + s_high
%   V_dc := given potential
%%%%%%%%%%%%%%%%%%%%%%%%%%%%%%%%%%%%%%%%

function [out] = tau(s_0,V_dc)

%%%%%%%%%%%%%%%%%%%%%%%%%%%%%%%%%%%%%%%%
% Constants
%%%%%%%%%%%%%%%%%%%%%%%%%%%%%%%%%%%%%%%%

  m_i = 40*1.67e-27; % [kg]
  e = 1.602e-19; % [C]

%%%%%%%%%%%%%%%%%%%%%%%%%%%%%%%%%%%%%%%%
% Calculations
%%%%%%%%%%%%%%%%%%%%%%%%%%%%%%%%%%%%%%%%

  out = 3*s_0*sqrt(m_i/(2*e*V_dc));

end
```

{sheath_parameters.m}

```
%%%%%%%%%%%%%%%%%%%%%%%%%%%%%%%%%%%%%%%%
% Calculate s_low & s_high
%   I_low  := low current
%   I_high := high current
%   f      := frequency
%   n      := integer
%   A      := area
%%%%%%%%%%%%%%%%%%%%%%%%%%%%%%%%%%%%%%%%
function [s_low,s_high] = sheath_parameters(I_low,I_high,f,n,A)

%%%%%%%%%%%%%%%%%%%%%%%%%%%%%%%%%%%%%%%%
% Constants
%%%%%%%%%%%%%%%%%%%%%%%%%%%%%%%%%%%%%%%%

  e = 1.602e-19; % [C]
  n_e = 1e16; % [m^-3]

%%%%%%%%%%%%%%%%%%%%%%%%%%%%%%%%%%%%%%%%
% Calculations
%%%%%%%%%%%%%%%%%%%%%%%%%%%%%%%%%%%%%%%%
```

```
  s_low = I_low/(e*n_e*2*pi*f*A);
  s_high = I_high/(e*n_e*2*pi*n*f*A);

end
```

{peak_currents.m}

```
%%%%%%%%%%%%%%%%%%%%%%%%%%%%%%%%%%%%%%%%
% Calculate I_low & I_high
%   x    := fraction of low freq. power
%   V_dc := given DC potential
%   f    := frequency
%   n    := integer
%   A    := area
%%%%%%%%%%%%%%%%%%%%%%%%%%%%%%%%%%%%%%%%

function [I_low,I_high] = peak_currents(x,V_dc,f,n,A)

%%%%%%%%%%%%%%%%%%%%%%%%%%%%%%%%%%%%%%%%
% Constants
%%%%%%%%%%%%%%%%%%%%%%%%%%%%%%%%%%%%%%%%

  e = 1.602e-19; % [C]
  epsilon_0 = 8.8542e-12; % [F/m]
  n_e = 1e16; % [m^-3]

%%%%%%%%%%%%%%%%%%%%%%%%%%%%%%%%%%%%%%%%
% Calculations
%
% sqrt([V]*[F/m]*[m^-3]*[s^-2]*[m^4])
% sqrt([V*F]/[s^2])
% sqrt([C]/[s^2])
%%%%%%%%%%%%%%%%%%%%%%%%%%%%%%%%%%%%%%%%

  I_low = x*sqrt(-8*pi^2*V_dc*epsilon_0*e*n_e*f^2*A^2);
  I_high = (1-x)*sqrt(-8*pi^2*V_dc*epsilon_0*e*n_e*(n*f)^2*A^2);

end
```

V_ion1 calls on the last three files to create the new ion voltage with the damping term accounted for. It is also the file that is altered for different parameters, such as: Vdc bias voltage, the area of the plates, the percent contribution between the low and high currents, and the electron density.

{V_ion1.m}

```
%%%%%%%%%%%%%%%%%%%%%%%%%%%%%%%%%%%%%%%%
% The monster function!
%   f := frequency
%   n := integer
%   phi := angle
%   t := instant in time
%%%%%%%%%%%%%%%%%%%%%%%%%%%%%%%%%%%%%%%%

function [out] = V_ion1(f,n,phi,t)

%%%%%%%%%%%%%%%%%%%%%%%%%%%%%%%%%%%%%%%%
```

```
% Constants
%%%%%%%%%%%%%%%%%%%%%%%%%%%%%%%%%%%%%%

  V_dc = 1000; % V
  A = pi*75e3^2; % m^2
  x = 0.5; % m

  e = 1.602e-19; % [C]
  n_e = 1e16; % m^-3
  epsilon_0 = 8.854e-12; % F/m

%%%%%%%%%%%%%%%%%%%%%%%%%%%%%%%%%%%%%%
% Calculations
%%%%%%%%%%%%%%%%%%%%%%%%%%%%%%%%%%%%%%

  [I_low,I_high] = peak_currents(x,-V_dc,f,n,A); % A
  [s_low,s_high] = sheath_parameters(I_low,I_high,f,n,A); % m
  tau_i = tau(s_low+s_high,V_dc); % s

%%%%%%%%%%%%%%%%%%%%%%%%%%%%%%%%%%%%%%
% The big function
%%%%%%%%%%%%%%%%%%%%%%%%%%%%%%%%%%%%%%

  f1 = e*n_e/(2*epsilon_0);
  terms(1) = 3*s_low^2/2;
  terms(2) = 3*s_high^2/2;
  terms(3) = 2*s_low*s_high;
  terms(4) = 2*s_low*(s_low + s_high)*sin(2*pi*f*t)/(2*pi*f*tau_i);
  terms(5) = 2*s_high*(s_low + s_high)*sin(2*pi*f*n*t + phi)/(2*pi*f*n*tau_i);
  terms(6) = -s_high^2*cos(2*2*pi*f*n*t + 2*phi)/(4*2*pi*f*n*tau_i);
  terms(7) = s_low*s_high*cos(2*pi*f*t*(n-1) + phi)/(2*pi*f*(n-1)*tau_i);
  terms(8) = s_low*s_high*cos(2*pi*f*t*(n+1) + phi)/(2*pi*f*(n+1)*tau_i);


  out = f1*sum(terms);

end
```

{IEDF.m}

```
%%%%%%%%%%%%%%%%%%%%%%%%%%%%%%%%%%%%%%
% Calculates the IEDF for given values
%   f   := frequency
%   n   := integer
%   phi := angle
%   t   := vector containing time values
%%%%%%%%%%%%%%%%%%%%%%%%%%%%%%%%%%%%%%

function [out,bins] = IEDF(f,n,phi,t)

%%%%%%%%%%%%%%%%%%%%%%%%%%%%%%%%%%%%%%
% Convenience:
%   You can just type "2" for f
%   and we will automatically multiply
%   by 1e6
%%%%%%%%%%%%%%%%%%%%%%%%%%%%%%%%%%%%%%
```

```
  if(f <= 100)
    f = f*1e6;
  end

%%%%%%%%%%%%%%%%%%%%%%%%%%%%%%%%%%%%%%%%%%%%%%%%%%%%%%%%%%%%%%%%%%%%%%%%%%%%%%%%%%%%%%%%%%
% Calculations
%%%%%%%%%%%%%%%%%%%%%%%%%%%%%%%%%%%%%%%%%%%%%%%%%%%%%%%%%%%%%%%%%%%%%%%%%%%%%%%%%%%%%%%%%%

  Y = arrayfun(@(x)V_ion1(f,n,phi,x),t);
  [out,bins] = hist(Y,500); % change this for higher fidelity

end
```

Frequency.m and Phase.m create the actual plots. Frequency.m depicts how distribution appears at a specific phase, harmonic, and frequency selection.

{Frequency.m}

```
close all
%%%% Change these (they affect the name of the file)
f=13.56e6;
n=2;
phi=1*pi/4;
fr=f;
phase=(phi/pi);


NR=length(f);

MAX=0;
MIN=Inf;
for ii=1:NR
    t_n = 10023; % Change this for higher fidelity
    t_max = 100/f(ii);
    t = 0:t_max/t_n:t_max;

    [vals,bins] = IEDF(13.56,n,phi,t);

    NDP(ii)=length(vals);
    T1(1:NDP(ii),ii)=vals;
    T2(1:NDP(ii),ii)=bins;
    T3(ii)=f(ii);

    if MIN>min(bins)
        MIN=min(bins);
    end

    if MAX<max(bins)
        MAX=max(bins);
    end
end
NDPN=max(NDP);
T4=linspace(MIN*.8,MAX*1.2,NDPN);

save('FILE_NAME.mat','T1','T2','T3')
load('FILE_NAME.mat')

for ii=1:NR
```

```
    T5(1:NDPN,ii)=interp1(T2(1:NDP(ii),ii),T1(1:NDP(ii),ii),T4,'linear',0);
end

col={'k','b','r','y','c','m','g','k','b','r','y','c','m','g'};
figure
hold on
for ii=1:NR
    plot3(T3(ii)*ones(NDPN,1),T4(1:NDPN),T5(1:NDPN,ii),'r','LineWidth',1)
    grid
    xlabel('Frequency (MHz)')
    ylabel('Voltage (V)')
    zlabel('Counts (%)')
end
hold off
set(gca,'Color','k')
view(3)

saveas(gca,['(n,p)\',num2str(fr/1e6),'_',num2str(n),'_',num2str(phase),'pi','.fig'],'fig')
print('-dmfile',['(n,p)\',num2str(fr/1e6),'_',num2str(n),'_',num2str(phase),'pi','.fig'])

figure
surf(T3(1:NR),T4(1:NDPN),T5(1:NDPN,1:NR),'LineStyle','none','Facecolor','interp')


figure
contourf(T3(1:NR),T4(1:NDPN),T5(1:NDPN,1:NR))
```

Phase.m depicts a top down view of how the distribution changes over the entire range of phase as frequency and harmonic selection stay constant.

{Phase.m}

```
close all

%number of runs
NR=360;

%freq
f(1:NR)=10e6;

%number of harmonics
n=2;

%start and finish phase is degrees
phi_start=0;
phi_fin=2*pi;

%phase
phi=linspace(phi_start,phi_fin,NR);

fr=f;

MAX=0;
MIN=Inf;
NDP(1:NR)=0;
X(1:NR)=0;
Y_TEMP(1:50000,1:NR)=0;
Z_TEMP(1:50000,1:NR)=0;
```

```
for ii=1:NR
    t_n = 10023; % Change this for higher fidelity
    t_max = 100/f(ii);
    t = 0:t_max/t_n:t_max;

    [vals,bins] = IEDF(13.56,n,phi(ii),t);

    NDP(ii)=length(vals);
    Z_TEMP(1:NDP(ii),ii)=vals;
    Y_TEMP(1:NDP(ii),ii)=bins;
    X(ii)=phi(ii);

    if MIN>min(bins)
        MIN=min(bins);
    end

    if MAX<max(bins)
        MAX=max(bins);
    end
end
NDPN=max(NDP);
Y=linspace(MIN*.8,MAX*1.2,NDPN);

Z(1:NDPN,1:NR)=0;
for ii=1:NR
   Z(1:NDPN,ii)=interp1(Y_TEMP(1:NDP(ii),ii),Z_TEMP(1:NDP(ii),ii),Y,'linear',0);
end

col={'k','b','r','y','c','m','g','k','b','r','y','c','m','g'};
 figure
 hold on
for ii=1:NR
    plot3(X(ii)*ones(NDPN,1)*180/pi,Y(1:NDPN),Z(1:NDPN,ii),'r','LineWidth',2)
    grid
    xlabel('Phase (degrees)','FontWeight','Bold','FontSize',12)
    ylabel('Voltage (V)','FontWeight','Bold','FontSize',12)
    zlabel('Counts (%)','FontWeight','Bold','FontSize',12)
end
hold off
set(gca,'Color','k','FontWeight','Bold','FontSize',12)
view(3)


 figure
 surf(X(1:NR),Y(1:NDPN),Z(1:NDPN,1:NR),'LineStyle','none','Facecolor','interp')
 xlabel('Phase [Log Scale]','FontWeight','Bold','FontSize',12)
 ylabel('Voltage (V)','FontWeight','Bold','FontSize',12)
 zlabel('Counts (%)','FontWeight','Bold','FontSize',12)


figure
Z_CON=Z+1;
contourf(X(1:NR),Y(1:NDPN),10*log10(Z_CON(1:NDPN,1:NR)))
title('Counts (arbitrary units)','FontWeight','Bold','FontSize',36)
xlabel('Phase (radians)','FontWeight','Bold','FontSize',24)
ylabel('Voltage (V)','FontWeight','Bold','FontSize',24)
colorbar
set(gca,'FontWeight','Bold','FontSize',30)
```

Appendix C

Vacuum System Equipment

Table 4: Equipment and their relevant information used within system set-up.

	COMPANY	MODEL #	NAME / PHYSICAL CHARACTERISTICS
Baratron	MKS	628B01TQE	Type 628B Baratron Capacitance Manometer
Langmuir Probe	Impedans	ALP-150	Automated Langmuir Probe System
Retarding Field Energy Analyzer (RFEA)	Impedans	SCU-800	Semion 800
Gate Valve	MDC	GV-4000M-P	N/A
Throttle Valve	MKS	653B-4-100-2	MKS Type 653B Exhaust Throttle Valve
Turbo Pump	BOC EDWARDS	STP iX455	Turbomolecular Pump
Roughing Pump	Leybold	D65B HE3	Trivac S65B Rotary Vane Vacuum Pump
Mass Flow Controller (MFC)	UNIT Instruments	URS-100-5	N/A
Pressure Controller	MKS	651CD2S1N	MKS Type 651C Pressure Controller
60 MHz Generator	Advanced Energy	3151278-000 A	N/A
60 MHz Match	Advanced Energy	3155168-002 F	RF Navigator
13.56 MHz Generator	Huttinger Electronic	PFG 300 RF	300W / 13.56MHz RF-OUTPUT
13.56 MHz Match	RFPP	7610807010	Auto Matching Network
Network Analyzer	RF Power Products (RFPP)	AMNPS-2A	N/A
V/I Probe	MKS	000-1106-113	N/A
V/I Probe Analyzer	MKS	000-1106-102	VI Probe Broadband Analysis
Computer (PC, 32-bit)	Dell & Microsoft	Optiplex 755	2.33 GHz Dual Core, 2 GB of RAM
Transmission Line 1	Pasternack Enterprises	RG393/U	87.6 cm
Transmission Line 2	Pasternack Enterprises	RG393/U	31.8 cm
Transmission Line 3	Pasternack Enterprises	RG393/U	125.7 cm
Transmission Line 4	Pasternack Enterprises	RG393/U	119.4 cm